Optimisation of pembrolizumab therapy for de novo metastatic MSI-H/dMMR colorectal cancer using data-driven delay integro-differential equations

Georgio Hawi[1, *], Peter S. Kim[1, †], and Peter P. Lee[2, †]

[1]School of Mathematics and Statistics, University of Sydney, Sydney, Australia
[2]Department of Immuno-Oncology, Beckman Research Institute, City of Hope, Duarte, California, USA
[*]Corresponding author: georgio.hawi@sydney.edu.au
[†]These authors contributed comparably to this work

Abstract

Colorectal cancer (CRC), the third most commonly diagnosed cancer worldwide, presents a growing public health concern, with 20% of new diagnoses involving de novo metastatic disease and up to 80% of these patients presenting with unresectable metastatic lesions. Microsatellite instability-high (MSI-H) CRC and deficient mismatch repair (dMMR) CRC constitute 15% of all CRC, and 4% of metastatic CRC, and, while less responsive to conventional chemotherapy, exhibit notable sensitivity to immunotherapy, especially programmed cell death protein 1 (PD-1) checkpoint inhibitors such as pembrolizumab. Despite this, there is a significant need to optimise immunotherapeutic regimens to maximise clinical efficacy and patient quality of life whilst minimising financial burden. In this work, we adapt the mechanistic model developed by Hawi et al. [arXiv:2411.12123 [q-bio.CB]] for locally advanced MSI-H/dMMR CRC to de novo metastatic MSI-H/dMMR CRC (dnmMCRC), deriving model parameters from pharmacokinetic, bioanalytical, and radiographic studies, as well as bulk RNA-sequencing data deconvolution from the TCGA COADREAD and GSE26571 datasets. We finally optimised treatment with pembrolizumab to balance efficacy, efficiency, and toxicity in dnmMCRC, comparing against currently FDA-approved regimens, analysing factors influencing treatment success and comparing immune dynamics to those in locally advanced disease.

Keywords: de novo metastatic MSI-H/dMMR colorectal cancer, pembrolizumab, delay integro-differential equations, treatment optimisation, systems biology, mechanistic model

1 Introduction

Colorectal cancer (CRC) is the third most common cancer worldwide, with more than 1.85 million cases and 850,000 deaths annually [1]. Of new CRC diagnoses, 20% of patients present with de novo metastatic disease, with an estimated 75%–90% of these patients presenting with unresectable metastatic lesions [2]. Furthermore, an additional 25% of patients who initially have localised disease eventually develop metastases [1]. However, since many people will not experience symptoms in the

early stages of CRC, diagnoses often occur at a later stage when the disease is more advanced, where treatment is less effective, and survival rates are significantly lower [3]. In the United States, the 5-year survival rates for stage IIIA, stage IIIB, and Stage IIIC colon cancer are 90%, 72%, and 53%, respectively, whilst stage IV CRC has a 5-year survival of only 12% [4].

Whilst many systemic therapies are available for advanced CRC, chemotherapy has been the main treatment approach, with mainstay chemotherapy regimens such as FOLFOX (folinic acid, 5-fluorouracil, oxaliplatin) and FOLFIRI (folinic acid, 5-fluorouracil, irinotecan) becoming integral to the treatment of advanced CRC [5]. However, patients with the hypermutant microsatellite instability-high (MSI-H) phenotype who have reached metastasis are less responsive to conventional chemotherapy and have a poorer prognosis compared to patients with microsatellite stable (MSS) CRC [6]. In particular, we note that in CRC, MSI-H and deficient mismatch repair (dMMR) tumours are equivalent [7], and we denote these tumours as MSI-H/dMMR for the remainder of this work. Approximately 20% of stage II, 12% of stage III, and 4% of stage IV CRC tumours are diagnosed as MSI-H/dMMR [8–10], with approximately 80% of sporadic MSI-H/dMMR CRC caused by MLH1 promoter hypermethylation [11]. This leads to a highly increased mutational rate, with MSI-H/dMMR CRC tumours having 10–100 times more somatic mutations compared to microsatellite stable (MSS) CRC tumours [12], resulting in increased tumour mutation burden (TMB) and neoantigen load, and immunogenic tumour microenvironment (TME) with dense immune cell infiltration [13, 14]. This immunogenicity results in patients with MSI-H/dMMR CRC having a good prognosis for immunotherapy treatment, in particular to immune checkpoint inhibitors (ICIs) [15].

Immune checkpoints, such as programmed cell death-1 (PD-1), cytotoxic T-lymphocyte-associated antigen 4 (CTLA-4), and lymphocyte-activation gene 3 (LAG-3), normally downregulate immune responses after antigen activation [16]. PD-1, a cell membrane receptor that is expressed on a variety of cell types, including activated T cells, activated B cells and monocytes, has been extensively researched in the context of cancer such as MSI-H/dMMR CRC [17, 18]. When PD-1 interacts with its ligands (PD-L1 and PD-L2), effector T cell activity is inhibited, resulting in the downregulation of pro-inflammatory cytokine secretion and the upregulation of immunosuppressive regulatory T cells (Tregs) [19, 20]. Cancers can exploit this by expressing PD-L1 themselves, evading immunosurveillance, and impairing the proliferation and activity of cytotoxic T lymphocytes (CTLs) [21]. Blockade of PD-1/PD-L1 complex formation reinvigorates effector T cell activity, resulting in enhanced anti-tumour immunity and responses, leading to improved clinical outcomes in cancer patients [22, 23].

The KEYNOTE-177 phase III trial, NCT02563002, aimed to evaluate the efficacy of first-line pembrolizumab, an anti-PD-1 antibody, in metastatic MSI-H/dMMR CRC (mMCRC) [11]. In the trial, 307 treatment-naive mMCRC patients were randomly assigned to receive pembrolizumab at a dose of 200 mg every 3 weeks or 5–fluorouracil–based chemotherapy every 2 weeks. A partial or complete response was observed in 43.8% of patients allocated to pembrolizumab therapy, compared with 33.1% of patients participating in 5-fluorouracil-based therapy. Furthermore, among patients who responded, 83% in the pembrolizumab group maintained response at 24 months, compared with 35% of patients receiving chemotherapy. These results motivated the FDA to approve pembrolizumab for the first-line treatment of unresectable or mMCRC on June 29, 2020 [24].

An important question to consider is the appropriate dosing and spacing of ICI therapies to balance tumour reduction with factors such as monetary cost, toxicity, and side effects [25, 26]. Mathematical models provide a powerful framework for optimising treatment regimens, whilst avoiding the significant time and financial costs associated with human clinical trials. There are numerous immunobiological

models of CRC, such as those from [27–30], and ICI therapy has been modelled extensively in other cancers, including those in [31–35]. Nonetheless, there are a multitude of limitations and drawbacks to these models of CRC and ICI therapy, as detailed in [36]. Additionally, to date, there are no pre-existing mathematical models in the literature for ICI therapy in de novo mMCRC (dnmMCRC). Furthermore, to the authors' knowledge, [36] presents the only immunobiological model of ICI therapy in CRC, and also addresses these drawbacks, focusing on the modelling and optimisation of neoadjuvant pembrolizumab therapy in locally advanced MSI-H/dMMR CRC (laMCRC). In this work, we adapt this model to dnmMCRC and use this to optimise pembrolizumab therapy as well as compare immune dynamics to those in laMCRC.

It is prudent for us to briefly outline, as repeated in [36], the functions and processes of some immune cells in the TME since their interaction with cancer cells directly or through chemokine/cytokine signalling significantly influences the efficacy of therapeutic regimens [37]. T cell activation occurs in the lymph node and occurs through T cell receptor (TCR) recognition of cancer antigen presented by major histocompatibility complex (MHC) class I molecules, in the case of CD8+ T cells, and MHC class II molecules, in the case of CD4+ T cells, expressed on the surfaces of mature DCs [38]. CTLs recognise cancer cells through TCR detection of peptide major histocompatibility complexes (pMHCs) on cancer cell surfaces via MHC class I [39]. CD8+ cells, as well as NK cells, are amongst the most cytotoxic and important cells in cancer cell lysis [40], in addition to secreting pro-inflammatory cytokines such as interleukin-2 (IL-2), interferon-gamma (IFN-γ), and tumour necrosis factor (TNF) [41]. These are also secreted by CD4+ T helper 1 (Th1) cells and are an important part of cell-mediated immunity, allowing for neutrophil chemotaxis and macrophage activation [42]. Furthermore, we must also consider Tregs, which are vital in immune tissue homeostasis since they are able to suppress the synthesis of pro-inflammatory cytokines and control intestinal inflammatory processes [43]. This is done in a variety of ways, including the production of immunomodulatory and immunosuppressive cytokines such as TGF-β, interleukin-10 (IL-10), and interleukin-35 (IL-35) [44, 45]. We note that naive CD4+ T cells can differentiate towards multiple additional phenotypes such as Th2, Th9, Th22, Tfh and Th17 cells, each involved in the pathogenesis of cancer [46, 47].

Also of importance in CRC are macrophages, which, like T cells, are able to produce pro-inflammatory and anti-inflammatory cytokines [48]. Naive macrophages, denoted M0 macrophages, can differentiate into two main phenotypes: classically activated M1 macrophages and alternatively activated M2 macrophages. These names were given since M1 macrophages promote Th1 cell responses, and M2 macrophages promote Th2 responses, with Th1-associated cytokines downregulating M2 activity, and vice versa [49]. M1 macrophages contribute to the inflammatory response by activating endothelial cells, promoting the induction of nitric oxide synthase, and producing large amounts of pro-inflammatory cytokines such as TNF, interleukin-1β (IL-1β), and IL-12 [50]. On the other hand, M2 macrophages are responsible for wound healing and the resolution of inflammation through phagocytosing apoptotic cells and releasing anti-inflammatory mediators such as IL-10, interleukin-13α1 (IL-13α1), and CC Motif Chemokine Ligand 17 (CCL17) [51].

It is important to note that the M1/M2 macrophage dichotomy is somewhat of a simplification. Macrophages are highly plastic and have been demonstrated to integrate environmental signals to change their phenotype and physiology [52]. To account for this, in the model, we incorporate macrophage polarisation and repolarisation between its anti-tumour and immunosuppressive phenotypes by various cytokines.

2 Mathematical Model

2.1 Model Variables and Assumptions

The variables and their units in the model are shown in Table 1.

Table 1: Variables used in the model. Quantities in the top box are in units of cell/cm^3, quantities in the second box are in units of g/cm^3, and all other quantities are in units of molec/cm^3. All quantities pertain to the tumour site unless otherwise specified. TDLN denotes the tumour-draining lymph node, whilst TS denotes the tumour site.

Var	Description	Var	Description
V_{TS}	Primary tumour volume		
C	Viable cancer cell density	N_c	Necrotic cell density
D_0	Immature DC density	D	Mature DC density in the TS
D^{LN}	Mature DC density at TDLN	T_0^8	Naive CD8+ T cell density in the TDLN
T_A^8	Effector CD8+ T cell density in the TDLN	T_8	Effector CD8+ T cell density in the TS
T_{ex}	Exhausted CD8+ T cell density in the TS	T_0^4	Naive CD4+ T cell density in the TDLN
T_A^1	Effector Th1 cell density in the TDLN	T_1	Effector Th1 cell density in the TS
T_0^r	Naive Treg density in the TDLN	T_A^r	Effector Treg density in the TDLN
T_r	Effector Treg density in the TS	M_0	Naive macrophage density
M_1	M1 macrophage density	M_2	M2 macrophage density
K_0	Naive NK cell density	K	Activated NK cell density
H	HMGB1 concentration	S	Calreticulin concentration
I_2	IL-2 concentration	I_γ	IFN-γ concentration
I_α	TNF concentration	I_β	TGF-β concentration
I_{10}	IL-10 concentration		
$P_D^{T_8}$	Unbound PD-1 receptor concentration on effector CD8+ T cells in the TS	$P_D^{T_1}$	Unbound PD-1 receptor concentration on effector Th1 cells in the TS
P_D^K	Unbound PD-1 receptor concentration on activated NK cells	$Q_A^{T_8}$	PD-1/pembrolizumab complex concentration on effector CD8+ T cells in the TS
$Q_A^{T_1}$	PD-1/pembrolizumab complex concentration on effector Th1 cells in the TS	Q_A^K	PD-1/pembrolizumab complex concentration on activated NK cells
P_L	Unbound PD-L1 concentration in the TS	Q^{T_8}	PD-1/PD-L1 complex concentration on effector CD8+ T cells in the TS
Q^{T_1}	PD-1/PD-L1 complex concentration on effector Th1 cells in the TS	Q^K	PD-1/PD-L1 complex concentration on activated NK cells
A_1	Concentration of pembrolizumab in the TS		
$P_D^{8\text{LN}}$	Unbound PD-1 receptor concentration on effector CD8+ T cells in the TDLN	$P_D^{1\text{LN}}$	Unbound PD-1 receptor concentration on effector Th1 cells in the TDLN
$Q_A^{8\text{LN}}$	PD-1/pembrolizumab complex concentration on effector CD8+ T cells in the TDLN	$Q_A^{1\text{LN}}$	PD-1/pembrolizumab complex concentration on effector Th1 cells in the TDLN
P_L^{LN}	Unbound PD-L1 concentration in the TDLN	$Q^{8\text{LN}}$	PD-1/PD-L1 complex concentration on effector CD8+ T cells in the TDLN
$Q^{1\text{LN}}$	PD-1/PD-L1 complex concentration on effector Th1 cells in the TDLN	A_1^{LN}	Concentration of pembrolizumab in the TDLN

For simplicity, we ignore spatial effects in the model, ignoring the effects of diffusion, advection, and chemotaxis by all species. We assume the system has two compartments: one at the TS, located in the colon or rectum, and one at the tumour-draining lymph node (TDLN). This is a simplification since

dnmMCRC typically involves multiple tumour-draining lymph nodes [53]; however, for simplicity, we focus on the sentinel node and refer to it as the TDLN for the purposes of the model. In a similar fashion to nearly all models of de novo metastatic cancer, we primarily focus on the growth of the primary tumour, using it as a proxy to infer the progression of lymph node and distant metastases. We assume that cytokines in the TS are produced only by effector or activated cells and that DAMPs in the TS are only produced by necrotic cancer cells. We assume that all mature DCs in the TDLN are cancer-antigen-bearing and that all T cells in the TS are primed with cancer antigens. Furthermore, we assume that all activated T cells in the TDLN are activated with cancer antigens and that T cell proliferation/division follows a deterministic program. We ignore CD4+ and CD8+ memory T cells and assume that naive CD4+ T cells differentiate immediately upon activation. We also assume that all Tregs in the TS are natural Tregs (nTregs), ignoring induced Tregs (iTregs). We assume, for simplicity, that activated macrophages polarise into the M1/M2 dichotomy. We also assume that the duration of pembrolizumab infusion is negligible compared to the timescale of the model. Therefore, we treat their infusions as an intravenous bolus so that drug absorption occurs immediately after infusion. Finally, we assume a constant solution history, where the history for each species is set to its respective initial condition.

We assume that all species, X_i, degrade/die at a rate proportional to their concentration, with decay constant d_{X_i}. We assume that the rate of activation/polarisation of a species X_i by a species X_j follows the Michaelis-Menten kinetic law $\lambda_{X_iX_j} X_i \frac{X_j}{K_{X_iX_j}+X_j}$, for rate constant $\lambda_{X_iX_j}$, and half-saturation constant $K_{X_iX_j}$. Similarly, we model the rate of inhibition of a species X_i by a species X_j using a term with form $\lambda_{X_iX_j} \frac{X_i}{1+X_j/K_{X_iX_j}}$ for rate constant $\lambda_{X_iX_j}$, and half-saturation constant $K_{X_iX_j}$. Production of X_i by X_j is modelled using mass-action kinetics unless otherwise specified, so that the rate at which X_i is formed is given by $\lambda_{X_iX_j} X_j$ for some positive constant $\lambda_{X_iX_j}$. Finally, we assume that the rate of lysis of X_i by X_j follows mass-action kinetics in the case where X_j is a cell and follows Michaelis-Menten kinetics in the case where X_j is a cytokine.

2.2 Model Summary

We now outline some of the main processes accounted for in the model, with all processes and equations being explained in Appendix A.

1. Effector CD8+ T cells and NK cells induce apoptosis of cancer cells, with this being inhibited by TGF-β and the PD-1/PD-L1 complex. However, TNF and IFN-γ induce necroptosis of cancer cells, causing them to become necrotic before they are removed.

2. Necrotic cancer cells release DAMPs such as HMGB1 and calreticulin, which stimulate immature DCs to mature.

3. Some mature DCs migrate to the T cell zone of the TDLN and activate naive CD8+ and CD4+ T cells (including Tregs), with CD8+ T cell and Th1 cell activation being inhibited by Tregs and the PD-1/PD-L1 complex.

4. Activated T cells undergo clonal expansion and proliferate rapidly in the TDLN, with CD8+ T cell and Th1 cell proliferation being inhibited by Tregs and the PD-1/PD-L1 complex.

5. T cells that have completed proliferation migrate to the TS and perform effector functions including the production of pro-inflammatory (IL-2, IFN-γ, TNF) and immunosuppressive (TGF-β, IL-10) cytokines. Extended exposure to the cancer antigen can lead CD8+ T cells to become exhausted, however, this exhaustion can be reversed by pembrolizumab.

6. In addition, mature DCs, NK cells and macrophages secrete cytokines that can activate NK cells and polarise and repolarise macrophages into pro-inflammatory and immunosuppressive phenotypes.

7. Pembrolizumab infusion promotes the binding of unbound PD-1 receptors to pembrolizumab, forming the PD-1/pembrolizumab complex instead of the PD-1/PD-L1 complex. This reduces the inhibition of pro-inflammatory CD8+ and Th1 cell activation and proliferation while also reducing the inhibition of cancer cell lysis.

2.3 Model Equations

The model equations follow identically from [36], with the exception of V_{TS}, which is time-dependent as opposed to being constant. For completeness, we provide the mathematical model below, with a full derivation of the model being found in Appendix A. The model parameter values are estimated in Appendix C and are listed in Table C.2.

2.3.1 Equations for Cancer Cells, DAMPs, and DCs

$$\begin{aligned}\frac{dC}{dt} &= \underbrace{\lambda_C C\left(1-\frac{C}{C_0}\right)}_{\text{growth}} - \underbrace{\lambda_{CT_8} T_8 \frac{1}{1+I_\beta/K_{CI_\beta}} \frac{1}{1+Q^{T_8}/K_{CQ^{T_8}}} C}_{\substack{\text{elimination by } T_8 \\ \text{inhibited by } I_\beta \text{ and } Q^{T_8}}} - \underbrace{\lambda_{CK} K \frac{1}{1+I_\beta/K_{CI_\beta}} \frac{1}{1+Q^{K}/K_{CQ^{K}}} C}_{\substack{\text{elimination by } K \\ \text{inhibited by } I_\beta \text{ and } Q^{K}}} \\ &\quad - \underbrace{\lambda_{CI_\alpha} \frac{I_\alpha}{K_{CI_\alpha}+I_\alpha} C}_{\text{elimination by } I_\alpha} - \underbrace{\lambda_{CI_\gamma} \frac{I_\gamma}{K_{CI_\gamma}+I_\gamma} C}_{\text{elimination by } I_\gamma},\end{aligned} \tag{2.1}$$

$$\frac{dN_c}{dt} = \underbrace{\lambda_{CI_\alpha} \frac{I_\alpha}{K_{CI_\alpha}+I_\alpha} C}_{\text{Elimination by } I_\alpha} + \underbrace{\lambda_{CI_\gamma} \frac{I_\gamma}{K_{CI_\gamma}+I_\gamma} C}_{\text{Elimination by } I_\gamma} - \underbrace{d_{N_c} N_c}_{\text{Removal}}. \tag{2.2}$$

$$\begin{aligned}\frac{dV_{\text{TS}}}{dt} &= \frac{1}{f_C+f_{N_c}}\left[\lambda_C f_C V_{\text{TS}}\left(1-\frac{f_C V_{\text{TS}}}{C_0}\right) - \lambda_{CT_8} T_8 \frac{1}{1+I_\beta/K_{CI_\beta}} \frac{1}{1+Q^{T_8}/K_{CQ^{T_8}}} f_C V_{\text{TS}}\right. \\ &\quad \left. -\lambda_{CK} K \frac{1}{1+I_\beta/K_{CI_\beta}} \frac{1}{1+Q^{K}/K_{CQ^{K}}} f_C V_{\text{TS}} - d_{N_c} f_{N_c} V_{\text{TS}}\right],\end{aligned} \tag{2.3}$$

where $C(t) = f_C V_{\text{TS}}(t)$ and $N_c(t) = f_{N_c} V_{\text{TS}}(t)$.

$$\frac{dH}{dt} = \underbrace{\lambda_{HN_c} N_c}_{\text{production by } N_c} - \underbrace{d_H H}_{\text{degradation}}, \tag{2.4}$$

$$\frac{dS}{dt} = \underbrace{\lambda_{SN_c} N_c}_{\text{production by } N_c} - \underbrace{d_S S}_{\text{degradation}}, \tag{2.5}$$

$$\frac{dD_0}{dt} = \underbrace{\mathcal{A}_{D_0}}_{\text{source}} - \underbrace{\lambda_{DH} D_0 \frac{H}{K_{DH}+H}}_{D_0 \to D \text{ by } H} - \underbrace{\lambda_{DS} D_0 \frac{S}{K_{DS}+S}}_{D_0 \to D \text{ by } S} - \underbrace{\lambda_{D_0K} D_0 K \frac{1}{1+I_\beta/K_{D_0I_\beta}}}_{\substack{\text{elimination by } K \\ \text{inhibited by } I_\beta}} - \underbrace{d_{D_0} D_0}_{\text{death}}, \tag{2.6}$$

$$\frac{dD}{dt} = \underbrace{\lambda_{DH} D_0 \frac{H}{K_{DH} + H}}_{D_0 \to D \text{ by } H} + \underbrace{\lambda_{DS} D_0 \frac{S}{K_{DS} + S}}_{D_0 \to D \text{ by } S} - \underbrace{\lambda_{DD^{\mathrm{LN}}} D}_{\substack{D \text{ migration} \\ \text{to TDLN}}} - \underbrace{d_D D}_{\text{death}}, \tag{2.7}$$

$$\frac{dD^{\mathrm{LN}}}{dt} = \frac{V_{\mathrm{TS}}}{V_{\mathrm{LN}}} \underbrace{\lambda_{DD^{\mathrm{LN}}} e^{-d_D \tau_m} D(t - \tau_m)}_{D \text{ migration to TDLN}} - \underbrace{d_D D^{\mathrm{LN}}}_{\text{death}}. \tag{2.8}$$

A diagram encompassing the interactions of these components is shown in Figure 1.

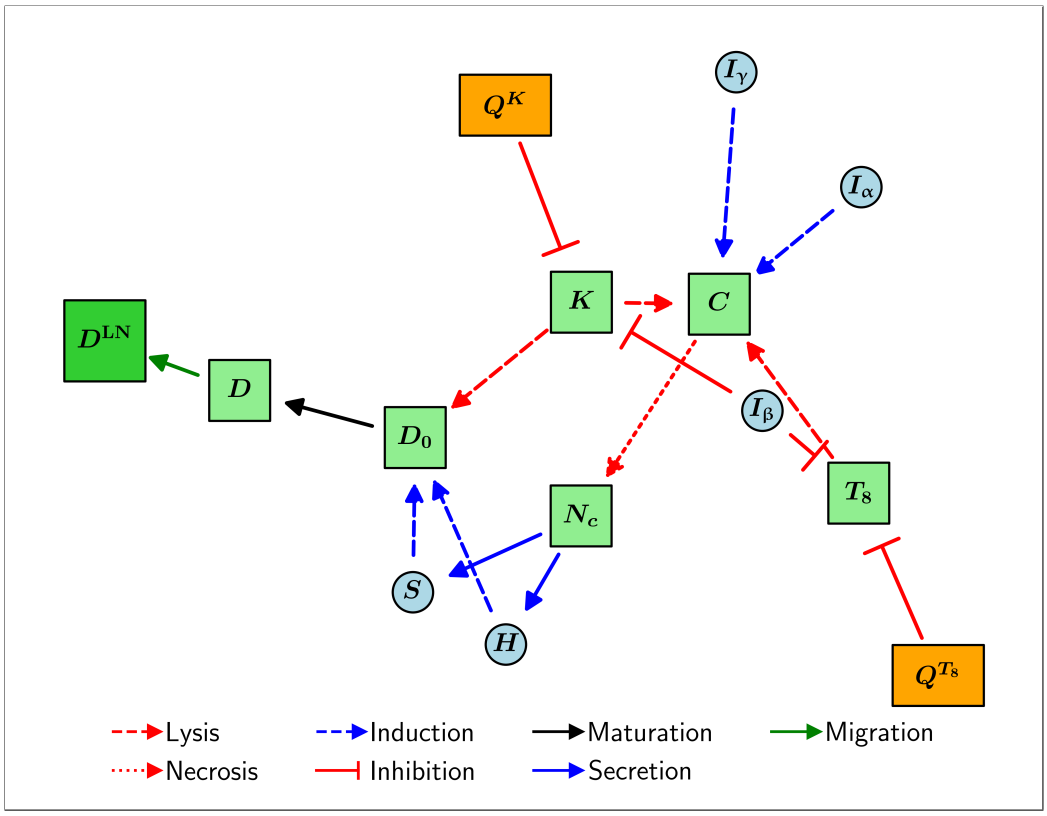

Figure 1: Schematic diagram of the interactions of cancer cells, DAMPs, and DCs in the model.

2.3.2 Equations for T Cells

$$\frac{dT_0^8}{dt} = \underbrace{\mathcal{A}_{T_0^8}}_{\text{source}} - \underbrace{R^8(t)}_{\substack{\text{CD8+ T cell} \\ \text{activation}}} - \underbrace{d_{T_0^8} T_0^8}_{\text{death}}, \tag{2.9}$$

where $R^8(t)$ is defined as

$$R^8(t) := \underbrace{\frac{\lambda_{T_0^8 T_A^8} e^{-d_{T_0^8} \tau_8^{\mathrm{act}}} D^{\mathrm{LN}}(t - \tau_8^{\mathrm{act}}) T_0^8(t - \tau_8^{\mathrm{act}})}{\left(1 + \int_{t-\tau_8^{\mathrm{act}}}^{t} T_A^r(s)\, ds / K_{T_0^8 T_A^r}\right)\left(1 + \int_{t-\tau_8^{\mathrm{act}}}^{t} Q^{8\mathrm{LN}}(s)\, ds / K_{T_0^8 Q^{8\mathrm{LN}}}\right)}}_{\text{CD8+ T cell activation inhibited by } T_A^r \text{ and } Q^{8\mathrm{LN}}}. \tag{2.10}$$

$$\frac{dT_A^8}{dt} = \underbrace{\frac{2^{n^8_{\max}} e^{-d_{T_0^8}\tau_{T_A^8}} R^8(t-\tau_{T_A^8})}{\left(1+\int_{t-\tau_{T_A^8}}^t T_A^r(s)\ ds/K_{T_A^8T_A^r}\right)\left(1+\int_{t-\tau_{T_A^8}}^t Q^{8\mathrm{LN}}(s)\ ds/K_{T_A^8Q^{8\mathrm{LN}}}\right)}}_{\text{CD8+ T cell proliferation inhibited by } T_A^r \text{ and } Q^{8\mathrm{LN}}} - \underbrace{\lambda_{T_A^8T_8}T_A^8}_{\substack{T_A^8 \text{ migration}\\ \text{to the TS}}} - \underbrace{d_{T_8}T_A^8}_{\text{death}}, \tag{2.11}$$

where $\tau_{T_A^8}$ is defined as

$$\tau_{T_A^8} := \Delta_8^0 + (n^8_{\max}-1)\Delta_8. \tag{2.12}$$

$$\begin{aligned}\frac{dT_8}{dt} &= \frac{V_{\mathrm{LN}}}{V_{\mathrm{TS}}}\underbrace{\lambda_{T_A^8T_8}e^{-d_{T_8}\tau_a}T_A^8(t-\tau_a)}_{T_A^8 \text{ migration to the TS}} + \underbrace{\lambda_{T_8I_2}\frac{T_8I_2}{K_{T_8I_2}+I_2}\frac{1}{1+T_r/K_{T_8T_r}}}_{\text{growth by } I_2 \text{ inhibited by } T_r}\\ &\quad - \underbrace{\lambda_{T_8C}\frac{T_8\int_{t-\tau_l}^t C(s)\ ds}{K_{T_8C}+\int_{t-\tau_l}^t C(s)\ ds}}_{T_8\to T_{\mathrm{ex}} \text{ from } C \text{ exposure}} + \underbrace{\lambda_{T_{\mathrm{ex}}A_1}\frac{T_{\mathrm{ex}}A_1}{K_{T_{\mathrm{ex}}A_1}+A_1}}_{T_{\mathrm{ex}}\to T_8 \text{ by } A_1} - \underbrace{\frac{d_{T_8}T_8}{1+I_{10}/K_{T_8I_{10}}}}_{\substack{\text{death}\\ \text{inhibited by } I_{10}}},\end{aligned} \tag{2.13}$$

$$\frac{dT_{\mathrm{ex}}}{dt} = \underbrace{\lambda_{T_8C}\frac{T_8\int_{t-\tau_l}^t C(s)\ ds}{K_{T_8C}+\int_{t-\tau_l}^t C(s)\ ds}}_{T_8\to T_{\mathrm{ex}} \text{ from } C \text{ exposure}} - \underbrace{\lambda_{T_{\mathrm{ex}}A_1}\frac{T_{\mathrm{ex}}A_1}{K_{T_{\mathrm{ex}}A_1}+A_1}}_{T_{\mathrm{ex}}\to T_8 \text{ by } A_1} - \underbrace{\frac{d_{T_{\mathrm{ex}}}T_{\mathrm{ex}}}{1+I_{10}/K_{T_{\mathrm{ex}}I_{10}}}}_{\substack{\text{death}\\ \text{inhibited by } I_{10}}}. \tag{2.14}$$

$$\frac{dT_0^4}{dt} = \underbrace{\mathcal{A}_{T_0^4}}_{\text{source}} - \underbrace{R^1(t)}_{\text{Th1 cell activation}} - \underbrace{d_{T_0^4}T_0^4}_{\text{death}}, \tag{2.15}$$

where $R^1(t)$ is defined as

$$R^1(t) := \underbrace{\frac{\lambda_{T_0^4T_A^1}e^{-d_{T_0^4}\tau^4_{\mathrm{act}}}D^{\mathrm{LN}}(t-\tau^4_{\mathrm{act}})T_0^4(t-\tau^4_{\mathrm{act}})}{\left(1+\int_{t-\tau_4^{\mathrm{act}}}^t T_r^A(s)\ ds/K_{T_0^4T_A^r}\right)\left(1+\int_{t-\tau_4^{\mathrm{act}}}^t Q^{1\mathrm{LN}}(s)\ ds/K_{T_0^4Q^{1\mathrm{LN}}}\right)}}_{\text{Th1 cell activation inhibited by } T_A^r \text{ and } Q^{1\mathrm{LN}}}. \tag{2.16}$$

$$\frac{dT_A^1}{dt} = \underbrace{\frac{2^{n^1_{\max}} e^{-d_{T_0^4}\tau_{T_A^1}} R^1(t-\tau_{T_A^1})}{\left(1+\int_{t-\tau_{T_A^1}}^t Q^{1\mathrm{LN}}(s)\ ds/K_{T_A^1Q^{1\mathrm{LN}}}\right)\left(1+\int_{t-\tau_{T_A^1}}^t T_A^r(s)\ ds/K_{T_A^1T_A^r}\right)}}_{\text{Th1 cell proliferation inhibited by } T_A^r \text{ and } Q^{1\mathrm{LN}}} - \underbrace{\lambda_{T_A^1T_1}T_A^1}_{\substack{T_A^1 \text{ migration}\\ \text{to the TS}}} - \underbrace{d_{T_1}T_A^1}_{\text{death}}, \tag{2.17}$$

where $\tau_{T_A^1}$ is defined as

$$\tau_{T_A^1} := \Delta_1^0 + (n^1_{\max}-1)\Delta_1. \tag{2.18}$$

$$\frac{dT_1}{dt} = \frac{V_{\mathrm{LN}}}{V_{\mathrm{TS}}}\underbrace{\lambda_{T_A^1T_1}e^{-d_{T_1}\tau_a}T_A^1(t-\tau_a)}_{T_A^1 \text{ migration to the TS}} + \underbrace{\lambda_{T_1I_2}\frac{T_1I_2}{K_{T_1I_2}+I_2}\frac{1}{1+T_r/K_{T_1T_r}}}_{\text{growth by } I_2 \text{ inhibited by } T_r} - \underbrace{\lambda_{T_1T_r}T_1\frac{Q^{T_1}}{K_{T_1T_r}+Q^{T_1}}}_{T_1\to T_r \text{ by } Q^{T_1}} - \underbrace{d_{T_1}T_1}_{\text{death}}, \tag{2.19}$$

$$\frac{dT_0^r}{dt} = \underbrace{\mathcal{A}_{T_0^r}}_{\text{source}} - \underbrace{R^r(t)}_{\text{Treg activation}} - \underbrace{d_{T_0^r}T_0^r}_{\text{death}}, \tag{2.20}$$

where $R^r(t)$ is defined as

$$R^r(t) := \underbrace{\lambda_{T_0^r T_A^r} e^{-d_{T_0^r}\tau^r_{\text{act}}} D^{\text{LN}}(t-\tau^r_{\text{act}}) T_0^r(t-\tau^r_{\text{act}})}_{\text{Treg activation}}. \tag{2.21}$$

$$\frac{dT_A^r}{dt} = \underbrace{2^{n^r_{\max}} e^{-d_{T_0^r}\tau_{T_A^r}} R^r(t-\tau_{T_A^r})}_{\text{Treg proliferation}} - \underbrace{\lambda_{T_A^r T_r} T_A^r}_{\substack{T_A^r \text{ migration} \\ \text{to the TS}}} - \underbrace{d_{T_r} T_A^r}_{\text{death}}, \tag{2.22}$$

where $\tau_{T_A^r}$ is defined as

$$\tau_{T_A^r} := \Delta_r^0 + (n^r_{\max} - 1)\Delta_r. \tag{2.23}$$

$$\frac{dT_r}{dt} = \frac{V_{\text{LN}}}{V_{\text{TS}}} \underbrace{\lambda_{T_A^r T_r} e^{-d_{T_r}\tau_a} T_A^r(t-\tau_a)}_{T_A^r \text{ migration to the TS}} + \underbrace{\lambda_{T_1 T_r} T_1 \frac{Q^{T_1}}{K_{T_1 T_r} + Q^{T_1}}}_{T_1 \to T_r \text{ by } Q^{T_1}} - \underbrace{d_{T_r} T_r}_{\text{death}}. \tag{2.24}$$

A diagram encompassing the interactions of these components is shown in Figure 2.

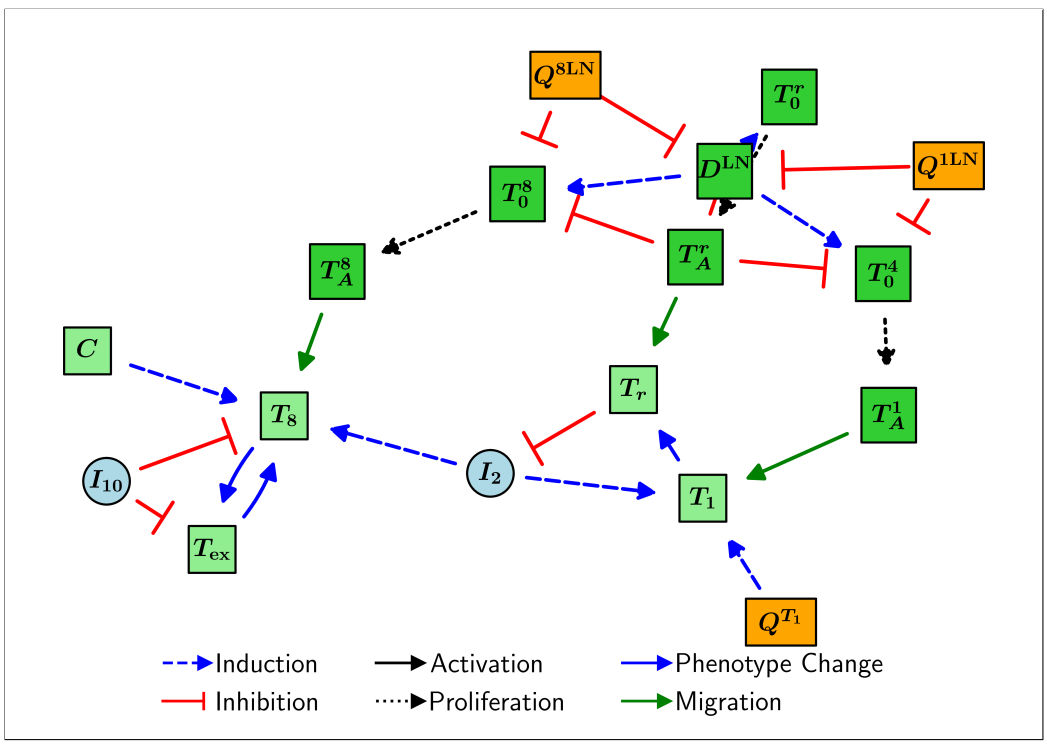

Figure 2: Schematic diagram of the interactions of T cells in the model.

2.3.3 Equations for Macrophages and NK Cells

$$\begin{aligned}\frac{dM_0}{dt} = {} & \underbrace{\mathcal{A}_{M_0}}_{\text{source}} - \underbrace{\lambda_{M_1 I_\alpha} M_0 \frac{I_\alpha}{K_{M_1 I_\alpha} + I_\alpha}}_{M_0 \to M_1 \text{ by } I_\alpha} - \underbrace{\lambda_{M_1 I_\gamma} M_0 \frac{I_\gamma}{K_{M_1 I_\gamma} + I_\gamma}}_{M_0 \to M_1 \text{ by } I_\gamma} - \underbrace{\lambda_{M_2 I_{10}} M_0 \frac{I_{10}}{K_{M_2 I_{10}} + I_{10}}}_{M_0 \to M_2 \text{ by } I_{10}} \\ & - \underbrace{\lambda_{M_2 I_\beta} M_0 \frac{I_\beta}{K_{M_2 I_\beta} + I_\beta}}_{M_0 \to M_2 \text{ by } I_\beta} - \underbrace{d_{M_0} M_0}_{\text{degradation}},\end{aligned} \tag{2.25}$$

$$\frac{dM_1}{dt} = \underbrace{\lambda_{M_1 I_\alpha} M_0 \frac{I_\alpha}{K_{M_1 I_\alpha} + I_\alpha}}_{M_0 \to M_1 \text{ by } I_\alpha} + \underbrace{\lambda_{M_1 I_\gamma} M_0 \frac{I_\gamma}{K_{M_1 I_\gamma} + I_\gamma}}_{M_0 \to M_1 \text{ by } I_\gamma} + \underbrace{\lambda_{M I_\gamma} M_2 \frac{I_\gamma}{K_{M I_\gamma} + I_\gamma}}_{M_2 \to M_1 \text{ by } I_\gamma} + \underbrace{\lambda_{M I_\alpha} M_2 \frac{I_\alpha}{K_{M I_\alpha} + I_\alpha}}_{M_2 \to M_1 \text{ by } I_\alpha}$$
$$- \underbrace{\lambda_{M I_\beta} M_1 \frac{I_\beta}{K_{M I_\beta} + I_\beta}}_{M_1 \to M_2 \text{ by } I_\beta} - \underbrace{d_{M_1} M_1}_{\text{degradation}} , \tag{2.26}$$

$$\frac{dM_2}{dt} = \underbrace{\lambda_{M_2 I_{10}} M_0 \frac{I_{10}}{K_{M_2 I_{10}} + I_{10}}}_{M_0 \to M_2 \text{ by } I_{10}} + \underbrace{\lambda_{M_2 I_\beta} M_0 \frac{I_\beta}{K_{M_2 I_\beta} + I_\beta}}_{M_0 \to M_2 \text{ by } I_\beta} - \underbrace{\lambda_{M I_\gamma} M_2 \frac{I_\gamma}{K_{M I_\gamma} + I_\gamma}}_{M_2 \to M_1 \text{ by } I_\gamma} - \underbrace{\lambda_{M I_\alpha} M_2 \frac{I_\alpha}{K_{M I_\alpha} + I_\alpha}}_{M_2 \to M_1 \text{ by } I_\alpha}$$
$$+ \underbrace{\lambda_{M I_\beta} M_1 \frac{I_\beta}{K_{M I_\beta} + I_\beta}}_{M_1 \to M_2 \text{ by } I_\beta} - \underbrace{d_{M_2} M_2}_{\text{degradation}} , \tag{2.27}$$

$$\frac{dK_0}{dt} = \underbrace{\mathcal{A}_{K_0}}_{\text{source}} - \left(\underbrace{\lambda_{K I_2} K_0 \frac{I_2}{K_{K I_2} + I_2}}_{K_0 \to K \text{ by } I_2} + \underbrace{\lambda_{K D_0} K_0 \frac{D_0}{K_{K D_0} + D_0}}_{K_0 \to K \text{ by } D_0} + \underbrace{\lambda_{K D} K_0 \frac{D}{K_{K D} + D}}_{K_0 \to K \text{ by } D} \right) \underbrace{\frac{1}{1 + I_\beta / K_{K I_\beta}}}_{\substack{\text{activation} \\ \text{inhibited by } I_\beta}} - \underbrace{d_{K_0} K_0}_{\text{degradation}} , \tag{2.28}$$

$$\frac{dK}{dt} = \left(\underbrace{\lambda_{K I_2} K_0 \frac{I_2}{K_{K I_2} + I_2}}_{K_0 \to K \text{ by } I_2} + \underbrace{\lambda_{K D_0} K_0 \frac{D_0}{K_{K D_0} + D_0}}_{K_0 \to K \text{ by } D_0} + \underbrace{\lambda_{K D} K_0 \frac{D}{K_{K D} + D}}_{K_0 \to K \text{ by } D} \right) \underbrace{\frac{1}{1 + I_\beta / K_{K I_\beta}}}_{\substack{\text{activation} \\ \text{inhibited by } I_\beta}} - \underbrace{d_K K}_{\text{degradation}} . \tag{2.29}$$

A diagram encompassing the interactions of these components is shown in Figure 3.

2.3.4 Equations for Cytokines

$$\frac{dI_2}{dt} = \underbrace{\lambda_{I_2 T_8} T_8}_{\text{production by } T_8} + \underbrace{\lambda_{I_2 T_1} T_1}_{\text{production by } T_1} - \underbrace{d_{I_2} I_2}_{\text{degradation}} . \tag{2.30}$$

After applying a quasi-steady-state approximation (QSSA), this becomes

$$I_2 = \frac{1}{d_{I_2}} \left(\lambda_{I_2 T_8} T_8 + \lambda_{I_2 T_1} T_1 \right) . \tag{2.31}$$

$$\frac{dI_\gamma}{dt} = \left(\underbrace{\lambda_{I_\gamma T_8} T_8}_{\text{production by } T_8} + \underbrace{\lambda_{I_\gamma T_1} T_1}_{\text{production by } T_1} \right) \underbrace{\frac{1}{1 + T_r / K_{I_\gamma T_r}}}_{\text{inhibition by } T_r} + \underbrace{\lambda_{I_\gamma K} K}_{\text{production by } K} - \underbrace{d_{I_\gamma} I_\gamma}_{\text{degradation}} . \tag{2.32}$$

After applying a QSSA, this becomes

$$I_\gamma = \frac{1}{d_{I_\gamma}} \left[\left(\lambda_{I_\gamma T_8} T_8 + \lambda_{I_\gamma T_1} T_1 \right) \frac{1}{1 + T_r / K_{I_\gamma T_r}} + \lambda_{I_\gamma K} K \right] . \tag{2.33}$$

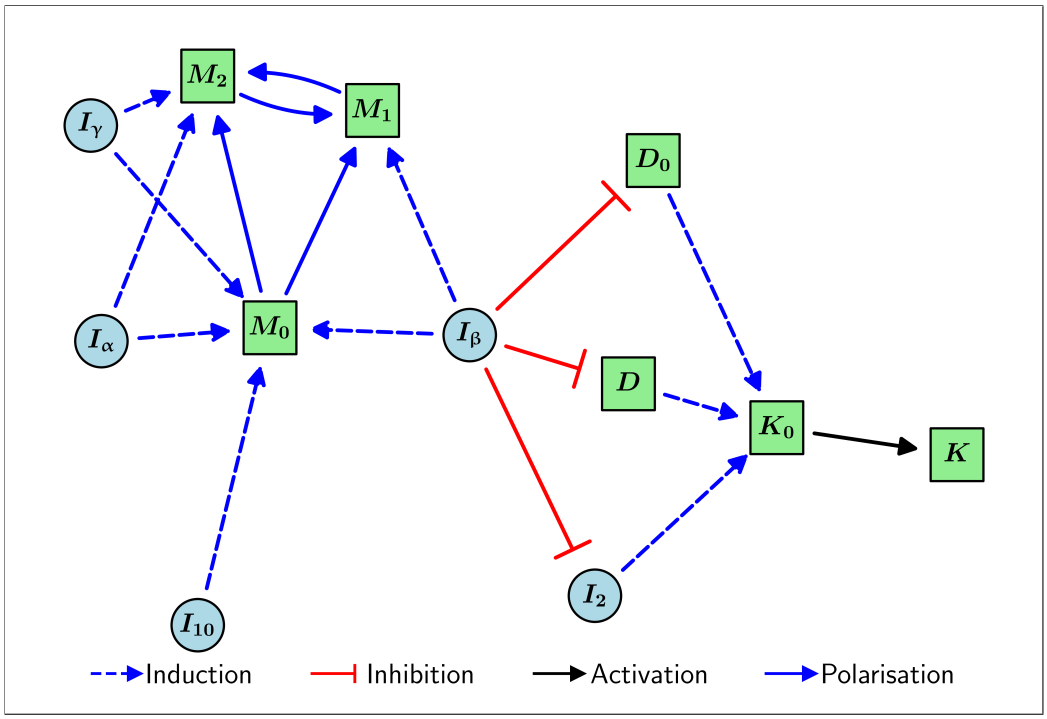

Figure 3: Schematic diagram of the interactions of macrophages and NK cells in the model.

$$\frac{dI_\alpha}{dt} = \underbrace{\lambda_{I_\alpha T_8} T_8}_{\text{production by } T_8} + \underbrace{\lambda_{I_\alpha T_1} T_1}_{\text{production by } T_1} + \underbrace{\lambda_{I_\alpha M_1} M_1}_{\text{production by } M_1} + \underbrace{\lambda_{I_\alpha K} K}_{\text{production by } K} - \underbrace{d_{I_\alpha} I_\alpha}_{\text{degradation}} . \tag{2.34}$$

After applying a QSSA, this becomes

$$I_\alpha = \frac{1}{d_{I_\alpha}} \left(\lambda_{I_\alpha T_8} T_8 + \lambda_{I_\alpha T_1} T_1 + \lambda_{I_\alpha M_1} M_1 + \lambda_{I_\alpha K} K \right) . \tag{2.35}$$

$$\frac{dI_\beta}{dt} = \underbrace{\lambda_{I_\beta C} C}_{\text{production by } C} + \underbrace{\lambda_{I_\beta T_r} T_r}_{\text{production by } T_r} + \underbrace{\lambda_{I_\beta M_2} M_2}_{\text{production by } M_2} - \underbrace{d_{I_\beta} I_\beta}_{\text{degradation}} . \tag{2.36}$$

After applying a QSSA, this becomes

$$I_\beta = \frac{1}{d_{I_\beta}} \left(\lambda_{I_\beta C} C + \lambda_{I_\beta T_r} T_r + \lambda_{I_\beta M_2} M_2 \right) . \tag{2.37}$$

$$\frac{dI_{10}}{dt} = \underbrace{\lambda_{I_{10} C} C}_{\text{production by } C} + \underbrace{\lambda_{I_{10} M_2} M_2}_{\text{production by } M_2} + \underbrace{\lambda_{I_{10} T_r} T_r \left(1 + \lambda_{I_{10} I_2} \frac{I_2}{K_{I_{10} I_2} + I_2} \right)}_{\text{production by } T_r \text{ enhanced by } I_2} - \underbrace{d_{I_{10}} I_{10}}_{\text{degradation}} . \tag{2.38}$$

A diagram encompassing the interactions of these components is shown in Figure 4.

2.3.5 Equations for Immune Checkpoint-Associated Components in the TS

$$\frac{dP_D^{T_8}}{dt} = \underbrace{\lambda_{P_D^{T_8}} T_8}_{\text{synthesis}} + \underbrace{\lambda_{Q_A} Q_A^{T_8}}_{\substack{\text{dissociation} \\ \text{of } Q_A^{T_8}}} - \underbrace{\lambda_{P_D A_1} P_D^{T_8} A_1}_{\text{binding to } A_1} - \underbrace{d_{P_D} P_D^{T_8}}_{\text{degradation}} , \tag{2.39}$$

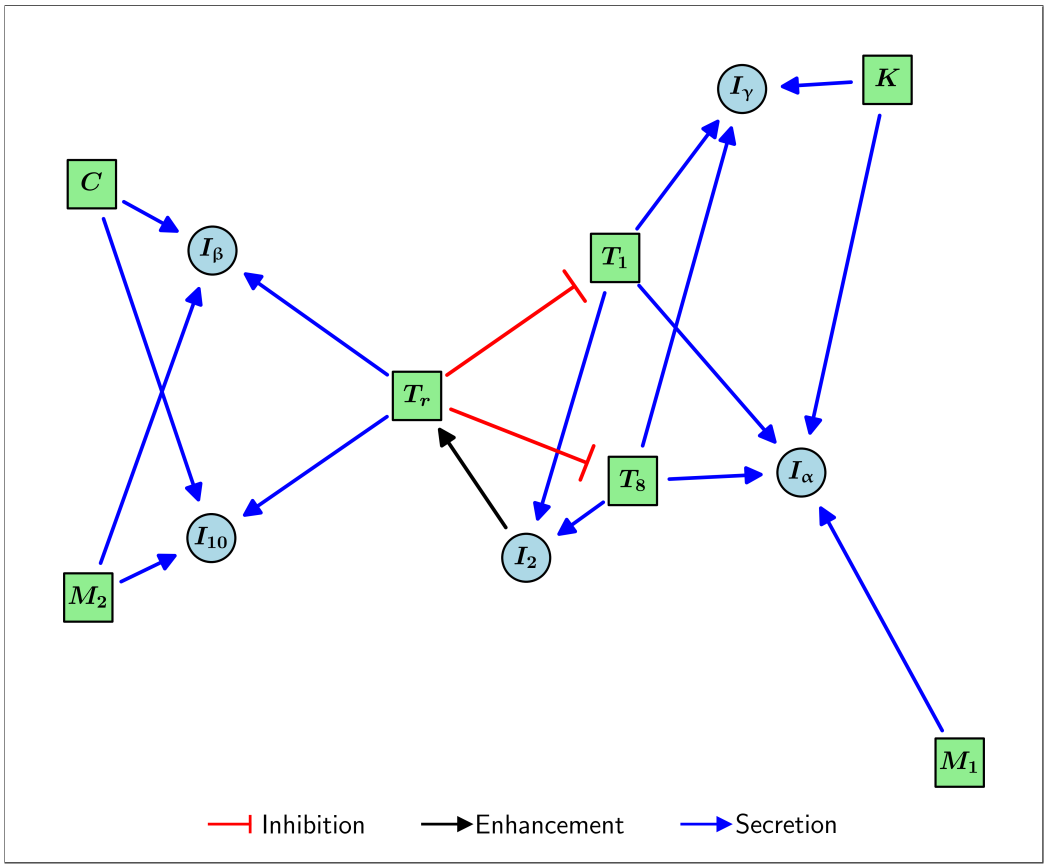

Figure 4: Schematic diagram of the interactions of cytokines in the model.

$$\frac{dP_D^{T_1}}{dt} = \underbrace{\lambda_{P_D^{T_1}} T_1}_{\text{synthesis}} + \underbrace{\lambda_{Q_A} Q_A^{T_1}}_{\substack{\text{dissociation}\\ \text{of } Q_A^{T_1}}} - \underbrace{\lambda_{P_D A_1} P_D^{T_1} A_1}_{\text{binding to } A_1} - \underbrace{d_{P_D} P_D^{T_1}}_{\text{degradation}} , \tag{2.40}$$

$$\frac{dP_D^{K}}{dt} = \underbrace{\lambda_{P_D^{K}} K}_{\text{synthesis}} + \underbrace{\lambda_{Q_A} Q_A^{K}}_{\substack{\text{dissociation}\\ \text{of } Q_A^{K}}} - \underbrace{\lambda_{P_D A_1} P_D^{K} A_1}_{\text{binding to } A_1} - \underbrace{d_{P_D} P_D^{K}}_{\text{degradation}} , \tag{2.41}$$

$$\frac{dQ_A^{T_8}}{dt} = \underbrace{\lambda_{P_D A_1} P_D^{T_8} A_1}_{\text{formation of } Q_A^{T_8}} - \underbrace{\lambda_{Q_A} Q_A^{T_8}}_{\text{dissociation of } Q_A^{T_8}} - \underbrace{d_{Q_A} Q_A^{T_8}}_{\text{internalisation}} , \tag{2.42}$$

$$\frac{dQ_A^{T_1}}{dt} = \underbrace{\lambda_{P_D A_1} P_D^{T_1} A_1}_{\text{formation of } Q_A^{T_1}} - \underbrace{\lambda_{Q_A} Q_A^{T_1}}_{\text{dissociation of } Q_A^{T_1}} - \underbrace{d_{Q_A} Q_A^{T_1}}_{\text{internalisation}} , \tag{2.43}$$

$$\frac{dQ_A^{K}}{dt} = \underbrace{\lambda_{P_D A_1} P_D^{K} A_1}_{\text{formation of } Q_A^{K}} - \underbrace{\lambda_{Q_A} Q_A^{K}}_{\text{dissociation of } Q_A^{K}} - \underbrace{d_{Q_A} Q_A^{K}}_{\text{internalisation}} , \tag{2.44}$$

$$\frac{dA_1}{dt} = \underbrace{\sum_{j=1}^{n} \xi_j f_{\text{pembro}} \delta\left(t - t_j\right)}_{\text{infusion}} + \underbrace{\lambda_{Q_A}\left(Q_A^{T_8} + Q_A^{T_1} + Q_A^{K}\right)}_{\text{dissociation of } Q_A^{T_8},\, Q_A^{T_1},\, \text{and } Q_A^{K}} - \underbrace{\lambda_{P_D A_1}\left(P_D^{T_8} + P_D^{T_1} + P_D^{K}\right) A_1}_{\text{formation of } Q_A^{T_8},\, Q_A^{T_1},\, \text{and } Q_A^{K}} - \underbrace{d_{A_1} A_1}_{\text{elimination}} , \tag{2.45}$$

$$\frac{dP_L}{dt} = \underbrace{\sum_{X \in \mathcal{X}} \lambda_{P_L X} X}_{\text{synthesis}} - \underbrace{d_{P_L} P_L}_{\text{degradation}}, \tag{2.46}$$

where $\mathcal{X} := \{C, D, T_8, T_1, T_r, M_2\}$.

$$Q^{T_8} = \frac{\lambda_{P_D P_L}}{\lambda_Q} P_D^{T_8} P_L, \tag{2.47}$$

$$Q^{T_1} = \frac{\lambda_{P_D P_L}}{\lambda_Q} P_D^{T_1} P_L, \tag{2.48}$$

$$Q^{K} = \frac{\lambda_{P_D P_L}}{\lambda_Q} P_D^{K} P_L. \tag{2.49}$$

A diagram encompassing the interactions of these components is shown in Figure 5.

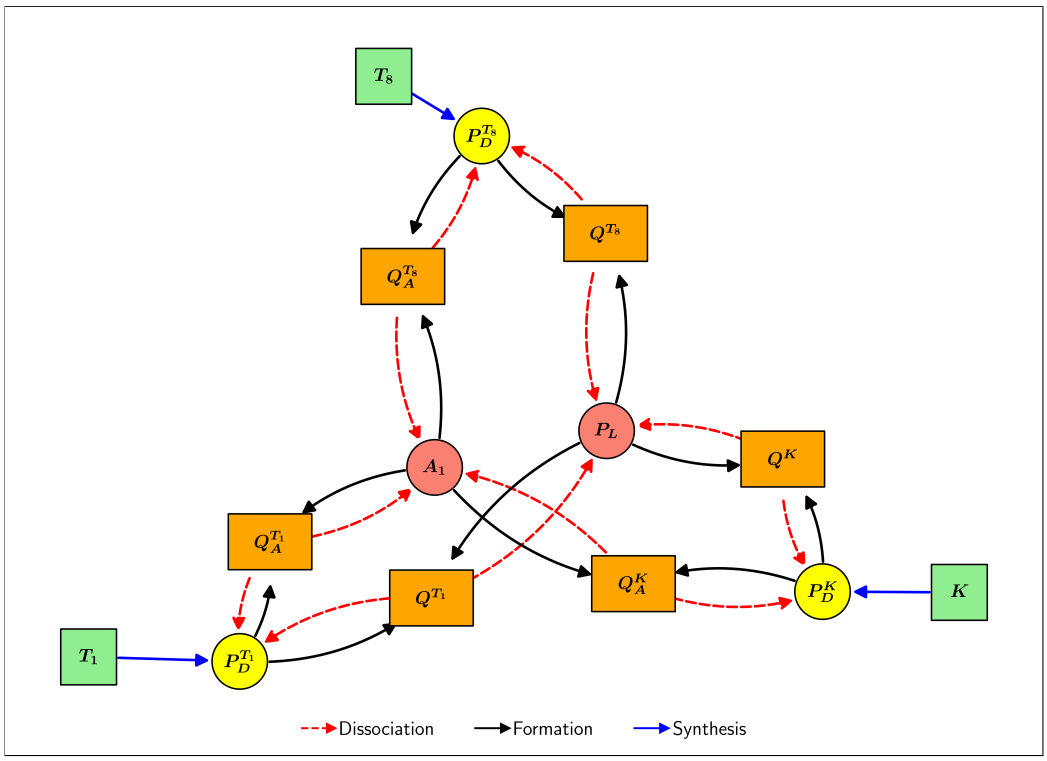

Figure 5: Schematic diagram of the interactions of immune checkpoint-associated components in the TS in the model.

2.3.6 Equations for Immune Checkpoint-Associated Components in the TDLN

$$\frac{dP_D^{8\text{LN}}}{dt} = \underbrace{\lambda_{P_D^{8\text{LN}}} T_A^8}_{\text{synthesis}} + \underbrace{\lambda_{Q_A} Q_A^{8\text{LN}}}_{\substack{\text{dissociation} \\ \text{of } Q_A^{8\text{LN}}}} - \underbrace{\lambda_{P_D A_1} P_D^{8\text{LN}} A_1^{\text{LN}}}_{\text{binding to } A_1^{\text{LN}}} - \underbrace{d_{P_D} P_D^{8\text{LN}}}_{\text{degradation}}, \tag{2.50}$$

$$\frac{dP_D^{1\text{LN}}}{dt} = \underbrace{\lambda_{P_D^{1\text{LN}}} T_A^1}_{\text{synthesis}} + \underbrace{\lambda_{Q_A} Q_A^{1\text{LN}}}_{\substack{\text{dissociation} \\ \text{of } Q_A^{1\text{LN}}}} - \underbrace{\lambda_{P_D A_1} P_D^{1\text{LN}} A_1^{\text{LN}}}_{\text{binding to } A_1^{\text{LN}}} - \underbrace{d_{P_D} P_D^{1\text{LN}}}_{\text{degradation}}, \tag{2.51}$$

$$\frac{dQ_A^{8\mathrm{LN}}}{dt} = \underbrace{\lambda_{P_D A_1} P_D^{8\mathrm{LN}} A_1^{\mathrm{LN}}}_{\text{formation of } Q_A^{8\mathrm{LN}}} - \underbrace{\lambda_{Q_A} Q_A^{8\mathrm{LN}}}_{\text{dissociation of } Q_A^{8\mathrm{LN}}} - \underbrace{d_{Q_A} Q_A^{8\mathrm{LN}}}_{\text{internalisation}}, \tag{2.52}$$

$$\frac{dQ_A^{1\mathrm{LN}}}{dt} = \underbrace{\lambda_{P_D A_1} P_D^{1\mathrm{LN}} A_1^{\mathrm{LN}}}_{\text{formation of } Q_A^{1\mathrm{LN}}} - \underbrace{\lambda_{Q_A} Q_A^{1\mathrm{LN}}}_{\text{dissociation of } Q_A^{1\mathrm{LN}}} - \underbrace{d_{Q_A} Q_A^{1\mathrm{LN}}}_{\text{internalisation}}, \tag{2.53}$$

$$\frac{dA_1^{\mathrm{LN}}}{dt} = \underbrace{\sum_{j=1}^{n} \xi_j f_{\mathrm{pembro}} \delta\left(t - t_j\right)}_{\text{infusion}} + \underbrace{\lambda_{Q_A}\left(Q_A^{8\mathrm{LN}} + Q_A^{1\mathrm{LN}}\right)}_{\text{dissociation of } Q_A^{8\mathrm{LN}} \text{ and } Q_A^{1\mathrm{LN}}} - \underbrace{\lambda_{P_D A_1}\left(P_D^{8\mathrm{LN}} + P_D^{1\mathrm{LN}}\right) A_1^{\mathrm{LN}}}_{\text{formation of } Q_A^{8\mathrm{LN}} \text{ and } Q_A^{1\mathrm{LN}}} - \underbrace{d_{A_1} A_1^{\mathrm{LN}}}_{\text{elimination}}, \tag{2.54}$$

$$\frac{dP_L^{\mathrm{LN}}}{dt} = \underbrace{\sum_{Y \in \mathcal{Y}} \lambda_{P_L^{\mathrm{LN}} Y} Y}_{\text{synthesis}} - \underbrace{d_{P_L} P_L^{\mathrm{LN}}}_{\text{degradation}}, \tag{2.55}$$

where $\mathcal{Y} := \left\{D^{\mathrm{LN}}, T_A^8, T_A^1, T_A^r\right\}$.

$$Q^{8\mathrm{LN}} = \frac{\lambda_{P_D P_L}}{\lambda_Q} P_D^{8\mathrm{LN}} P_L^{\mathrm{LN}}, \tag{2.56}$$

$$Q^{1\mathrm{LN}} = \frac{\lambda_{P_D P_L}}{\lambda_Q} P_D^{1\mathrm{LN}} P_L^{\mathrm{LN}}. \tag{2.57}$$

A diagram encompassing the interactions of these components is shown in Figure 6.

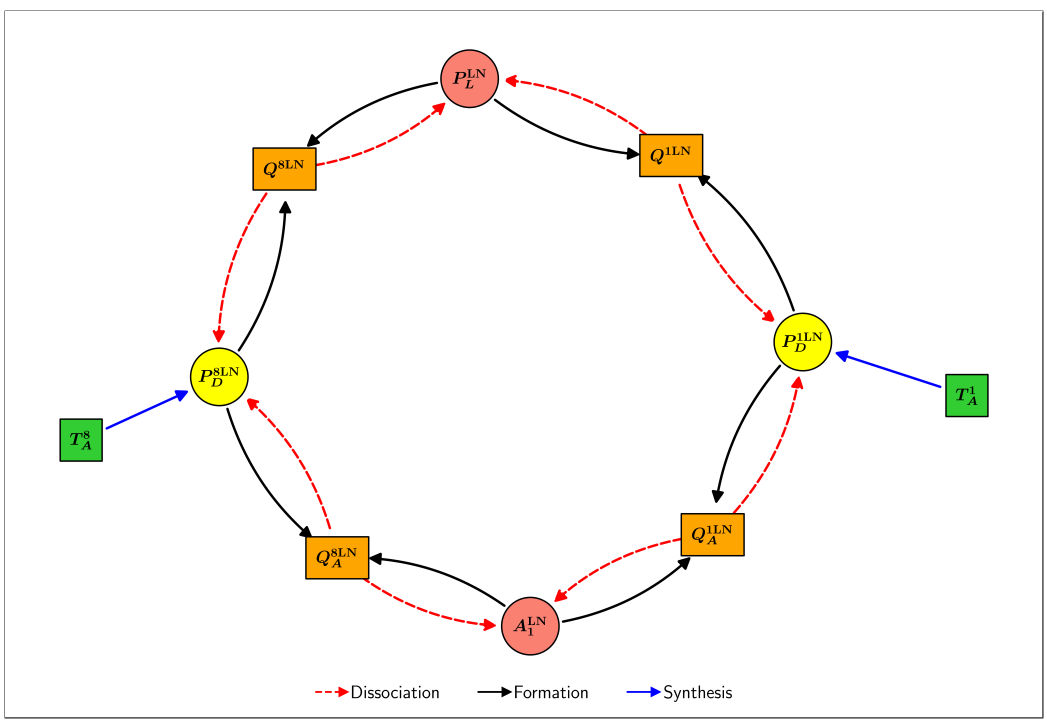

Figure 6: Schematic diagram of the interactions of immune checkpoint-associated components in the TDLN in the model.

3 Steady States and Initial Conditions

We estimated all steady states and initial conditions under the assumption that pembrolizumab has not been and will not be administered.

3.1 Steady States and Initial Conditions for Cells in the TS

Digital cytometry has proved itself to be a powerful technique in characterising immune cell populations from individual patients' bulk tissue transcriptomes without requiring physical cell isolation [54–58]. In particular, RNA-sequencing (RNA-seq) deconvolution of tumour gene expressions has been very useful in determining immune profiles and adjusting treatment accordingly. For all algorithms outlined in the sequel, we aggregate the estimates by taking the median of the relevant non-zero values elementwise and then normalising such that their sums become 1.

To estimate immune cell population proportions in dnmMCRC, we applied multiple algorithms and then synthesised their results to obtain estimates for all cell types in the model. We first used the ImmuCellAI algorithm [59], which estimates the abundance of 24 immune cell types from gene expression data and has also been shown to be highly accurate in predicting immunotherapy response. These immune cell types include 18 T cell subsets, including CD4+ T cells which incorporate T helper cells (namely Th1 cells, Th2 cells, Th17 cells, and T follicular helper cells), regulatory T cells (including natural Tregs (nTregs), induced Tregs (iTregs), and type 1 regulatory T cells (Tr1s)), naive CD4+ T cells (CD4_naive) and other CD4+ T cells (CD4_T). In addition, they include naive CD8+ T cells (CD8_T), CTLs (Tc), exhausted CD8+ T cells (Tex), central memory T cells (Tcm), effector memory T cells (Tem), natural killer T cells (NKT), $\gamma\delta$ T cells (Tgd), and mucosal-associated invariant T cells (MAIT). ImmuCellAI also estimates the abundance of DCs, B cells, monocytes, macrophages, and NK cells. Direct correspondences between state variables in the model and ImmuCellAI cell types are shown in Table B.1.

Using the UCSC Xena web portal [60], RSEM normalised RNA-seq gene expression profiles of patients from the TCGA COAD and TCGA READ projects [61] were acquired, featuring patients with colorectal adenocarcinomas. Corresponding clinical and biospecimen data were downloaded from the GDC portal [62] and included tumour dimensions, necrotic cell percentage, AJCC TNM stage, and MSIsensor and MANTIS MSI statuses. We filtered for samples from primary tumours and with non-empty necrosis percentage data from patients with AJCC stage IV CRC and at least one of MANTIS score > 0.4 or MSIsensor score $> 3.5\%$, as these are the default thresholds for MSI-H [63]. We performed 2-means clustering on the estimated cell proportions generated by ImmuCellAI to categorise samples into the stage IVA and stage IVB/IVC TNM stages. We considered only the 'NK', 'DC', nTreg', 'Th1', 'Cytotoxic', and 'Exhausted' cell types as part of the clustering, excluding macrophages because they consist of M0, M1, and M2 phenotypes, which are not differentiated by ImmuCellAI. To properly assign and label each cluster, we compared the individual coordinates of each cluster's centroid. Notably, stage IVB/IVC samples, corresponding to further CRC progression, are characterised by a higher proportion of DCs and nTregs, along with a lower proportion of Th1 cells, cytotoxic T cells, and NK cells compared to stage IVA samples. In particular, to infer steady states, we used stage IVB/IVC samples, whilst stage IVA samples were used to determine initial conditions. We also used the manually curated TIMEDB cell composition database [64] to source tumour deconvolution estimates for each relevant individual sample.

Additionally, the aggregated estimated cell proportions generated by ImmuCellAI for steady states

and initial conditions, after normalisation, are shown in Table B.2 and Table B.3.

To determine the proportions of M_0, M_1 and M_2, we used the CIBERSORTx algorithm [54], due to its high accuracy [65]. We followed a similar approach to [27] and [28] and applied CIBERSORTx B-mode on the refined gene expression data, using the validated LM22 signature matrix [58], which gave relative immune cell proportions of 22 immune cell types using 547 signature genes derived from microarray data. Direct correspondences between state variables in the model and keys of the LM22 signature matrix are shown in Table B.4. The aggregated estimated cell proportions generated by CIBERSORTx for steady states and initial conditions, after normalisation, are shown in Table B.5 and Table B.6.

However, to determine the proportions of D_0 and D, and K_0 and K, we could not use CIBERSORTx due to its nil results. Instead, we used a combination of biologically informed assumptions and data from physical experiments. It was determined in [66] that the ratio of the proportions of cytotoxic, activated NK cells to naive NK cells decreases as CRC progresses. We thus assume that, $K_0(0) = 10K(0)$, and that $\overline{K_0} = 20\overline{K}$. We also estimate that $D_0(0) \approx D(0)$, using [36] as a guide, and noting that cancer progression leads to increased DAMP production and DC maturation, assume that $\overline{D} = 2\overline{D_0}$.

We integrated the relative proportions within cell types for DCs, NK cells, and macrophages outputted by CIBERSORTx into the ImmuCellAI abundance estimates. We note that the density of immune cells in a healthy adult colon is approximately 3.37×10^7 cell/g [67], which assuming a tissue density of 1.03 g/cm^3, results in a total immune cell density of 3.47×10^7 cell/cm^3. However, advanced cancer induces lymphadenopathy [68, 69], which [67] estimates results in an increase in the total number of lymphocytes of at most 10%. As such, we assume that there is a 10% increase in lymphocyte concentration in dnmMCRC.

Accounting for the low immunogenicity of tumours in dnmMCRC, we followed [28] and assumed at steady state that the density of cancer cells is equal to double the total immune cell density. Taking into account lymphadenopathy and using data from [67], we assumed that the total immune cell density in dnmMCRC initially is approximately 3.70×10^7 cell/cm^3 and at steady state is approximately 3.69×10^7 cell/cm^3. As such, we are justified in assuming that the total immune cell density remains constant throughout the cancer's progression. From the TCGA biospecimen data, the median necrotic cancer cell percentage for stage IV MSI-H CRC samples is 5%. As such, denoting $\overline{\text{TIC}}$ as the total immune cell density at steady state, and N_p as the necrotic cell percentage, we have that

$$\overline{C} + \overline{N_c} = 2 \times \overline{\text{TIC}}, \tag{3.1}$$

$$\frac{\overline{N_c}}{N_p} = \frac{\overline{C}}{1 - N_p}, \quad \overline{C} = 2 \times \overline{\text{TIC}} \times (1 - N_p) \implies \overline{N_c} = 2 \times \overline{\text{TIC}} \times N_p. \tag{3.2}$$

Thus, at steady state, $C \approx 7.02 \times 10^7$ cell/cm^3 and $N_c \approx 3.69 \times 10^6$ cell/cm^3.

A retrospective cohort study by Burke et al. considered CRC patients at Leeds Teaching Hospitals NHS Trust over a 2-year interval who received no treatment and who underwent computed tomography (CT) scans twice, more than 5 weeks apart. It was found that in patients whose M category remained stable at M1, the median tumour doubling time for these patients was 213 days [70]. Furthermore, the mean tumour volume in stage IVA and stage IVB CRC patients was found to be 33.23 cm^3 and

59.87 cm^3, respectively [71]. Noting that fewer than 0.1% of disseminated cancer cells successfully form distant metastases [72], we assumed that the primary tumour volume in dnmMCRC remains close, if not slightly smaller, to these values. This corresponds to V_{TS} taking approximately 180.9 days to reach its steady-state value, and we assume this to be the case for C and N_c as well. This also corresponds to an initial condition for C being $C(0) = 3.90 \times 10^7$ cell/cm^3 and thus $N_c(0) \approx 2.05 \times 10^6$ cell/cm^3.

Combining everything, the resultant steady states and initial conditions for the model are shown in Table 2 and Table 3.

Table 2: TS steady-state cell densities for the model, combining estimates derived from ImmuCellAI and CIBERSORTx. All values are in cell/cm^3.

C	N_c	D_0	D	T_8	T_{ex}	T_1
7.02×10^7	3.69×10^6	9.55×10^5	1.91×10^6	1.77×10^5	1.24×10^5	1.06×10^5
T_r	M_0	M_1	M_2	K_0	K	
2.78×10^5	7.93×10^5	3.27×10^5	1.30×10^6	3.88×10^6	1.94×10^5	

Table 3: TS initial condition cell densities for the model, combining estimates derived from ImmuCellAI and CIBERSORTx. All values are in cell/cm^3.

C	N_c	D_0	D	T_8	T_{ex}	T_1
3.90×10^7	2.05×10^6	1.04×10^6	1.04×10^6	1.61×10^5	1.93×10^5	1.01×10^5
T_r	M_0	M_1	M_2	K_0	K	
2.02×10^5	2.50×10^5	2.09×10^5	1.29×10^6	4.47×10^6	4.47×10^5	

We note that, technically, ImmuCellAI is an enrichment-based method that does not provide absolute immune cell proportions but rather estimates abundances across various immune cell subtypes not reported by CIBERSORTx. However, normalising these abundances provides a good approximation of the true immune cell proportions, thereby allowing ImmuCellAI to be justifiably employed to estimate immune cell steady states and initial conditions.

3.2 Steady States and Initial Conditions for Cells in the TDLN

To determine the initial conditions and steady-state values for T_0^8, T_A^8, T_0^4, T_A^1, T_0^r, and T_A^r, we used ImmuCellAI on the GSE26571 dataset from the NCBI Gene Expression Omnibus repository [73, 74], obtaining deconvolution results from TIMEDB. This contains 9 samples of lymph node metastases from 7 patients with colon adenocarcinoma, with data from [75]. However, the dataset's metadata does not contain AJCC TNM stages for patients. To estimate the TNM stages of the patients with lymph node metastases, we considered the samples of lymph node metastases for these patients and applied the ImmuCellAI algorithm to estimate their immune cell abundances, ignoring Tcm and Tem cell subtypes. Mappings between ImmuCellAI immune cell types and TDLN cell types in the model are shown in Table B.7.

To distinguish lymph node metastases from stage IVA patients, with those with more advanced disease, we performed 2-means clustering on the estimated cell proportions generated by ImmuCellAI, following a similar approach to Section 3.1. In particular, we considered the 'nTreg', 'Th1', 'Th2', and 'Cytotoxic' cell types as part of the clustering. We, again, compare the individual coordinates

of each cluster's centroid and note that lymph node metastases from stage IVB/IVC samples, which correspond to more advanced CRC progression, exhibit a higher proportion of Th2 cells and nTregs, alongside a lower proportion of Th1 cells and cytotoxic T cells compared to stage IVA samples. Like before, we used lymph node metastases from stage IVB/IVC patients to infer TDLN steady states and those from stage IVA patients to infer initial conditions. Aggregating the estimates, as before, and then normalising such that their sums become 1, results in the proportions as shown in Table B.8 and Table B.9.

The density of immune cells in the lymph nodes of an adult is approximately 1.8×10^9 cell/g [67], which assuming a tissue density of 1.03 g/cm^3, results in a total immune cell density of 1.854×10^9 cell/cm^3. Finally, we assumed that in the TDLN, the number of activated CD8+ T cells having undergone $n^8_{\max}$ divisions is roughly half the number that has only undergone $n^8_{\max} - 1$ divisions and so forth. Furthermore, we assumed that initially, and at steady state, 10% of all Tregs are naive. Thus, we assume that for $i = 1, 8$,

$$T_A^i = \frac{2^{n^i_{\max}}}{2^{n^i_{\max}+1} - 1} T_A^{i\mathrm{LN}},$$

and that

$$T_0^r = \frac{T_A^{r\mathrm{LN}}}{10}, \quad T_A^r = \frac{9}{10} \frac{2^{n^r_{\max}}}{2^{n^r_{\max}+1} - 1} T_A^{r\mathrm{LN}},$$

where $T_A^{i\mathrm{LN}}$ is the total number of activated T cells in the TDLN of the corresponding type.

Combining everything, the resultant steady-states and initial conditions for the model are shown in Table 4 and Table 5, respectively.

Table 4: TDLN steady-state cell densities for the model, using estimates derived from ImmuCellAI. All values are in cell/cm^3.

T_0^8	T_A^8	T_0^4	T_A^1	T_0^r	T_A^r
1.16×10^7	8.31×10^5	6.73×10^6	6.66×10^6	3.23×10^5	1.47×10^6

Table 5: TDLN initial condition cell densities for the model, using estimates derived from ImmuCellAI. All values are in cell/cm^3.

T_0^8	T_A^8	T_0^4	T_A^1	T_0^r	T_A^r
1.20×10^7	8.60×10^5	4.31×10^6	7.76×10^6	1.72×10^5	7.81×10^5

Finally, we estimated the steady states and initial conditions for D^{LN} to be 3.28×10^7 cells/cm^3 and 1.78×10^7 cells/cm^3, respectively, with justification for the choice of these values as in Appendix C.9.1.

3.3 Steady States and Initial Conditions for DAMPs

We chose the DAMP steady states and initial conditions to be as in Table 6. Justification for the choice of these values is done in Appendix C.1.

Table 6: DAMP steady states and initial conditions for the model. All values are in units of g/cm^3.

DAMP	Steady State	Initial Condition
H	1.94×10^{-8}	1.33×10^{-8}
S	4.50×10^{-8}	3.25×10^{-8}

3.4 Steady States and Initial Conditions for Cytokines

We chose the cytokine steady states and initial conditions to be as in Table 7. Justification for the choice of these values is done in Appendix C.2.

Table 7: Cytokine steady states and initial conditions for the model. All values are in units of g/cm^3.

Cytokine	Steady State	Initial Condition
I_2	2.00×10^{-12}	1.87×10^{-12}
I_γ	4.93×10^{-11}	1.10×10^{-10}
I_α	9.00×10^{-11}	1.25×10^{-10}
I_β	1.51×10^{-6}	9.20×10^{-7}
I_{10}	1.84×10^{-10}	1.15×10^{-10}

3.5 Steady States and Initial Conditions for Immune Checkpoint-Associated Components in the TS

We choose the TS immune checkpoint-associated component steady states and initial conditions to be as in Table 8. Justification for the choice of these values is done in Appendix C.12.

Table 8: TS immune checkpoint-associated component steady states and initial conditions for the model. All values are in units of molec/cm^3.

Protein	Steady State	Initial Condition
$P_D^{T_8}$	4.87×10^8	4.44×10^8
$P_D^{T_1}$	2.17×10^8	2.07×10^8
P_D^K	1.07×10^8	2.46×10^8
P_L	1.30×10^{13}	7.40×10^{12}
Q^{T_8}	1.35×10^6	6.99×10^5
Q^{T_1}	6.01×10^5	3.26×10^5
Q^K	2.96×10^5	3.88×10^5

We also set the initial condition and steady states for all pembrolizumab-associated components in the TS to be 0, as shown in Table 9.

Table 9: Steady states and initial conditions for pembrolizumab-associated components in the TS in the model. All values are in units of molec/cm^3.

Protein	Steady State	Initial Condition
$Q_A^{T_8}$	0	0
$Q_A^{T_1}$	0	0
Q_A^K	0	0
A_1	0	0

3.6 Steady States and Initial Conditions for Immune Checkpoint-Associated Components in the TDLN

We choose the TDLN immune checkpoint-associated component steady states and initial conditions to be as in Table 10. Justification for the choice of these values is done in Appendix C.13.

Table 10: TDLN immune checkpoint-associated component steady states and initial conditions for the model. All values are in units of molec/cm^3.

Protein	Steady State	Initial Condition
$P_D^{8\text{LN}}$	2.29×10^9	2.37×10^9
$P_D^{1\text{LN}}$	1.37×10^{10}	1.59×10^{10}
P_L^{LN}	5.99×10^{11}	3.34×10^{11}
$Q^{8\text{LN}}$	2.92×10^5	1.69×10^5
$Q^{1\text{LN}}$	1.74×10^6	1.13×10^6

We also set the initial condition and steady states for all pembrolizumab-related quantities in the TDLN to be 0, as shown in Table 11.

Table 11: Steady states and initial conditions for pembrolizumab-associated components in the TDLN in the model. All values are in units of molec/cm^3.

Protein	Steady State	Initial Condition
$Q_A^{8\text{LN}}$	0	0
$Q_A^{1\text{LN}}$	0	0
A_1^{LN}	0	0

4 Results

We now aim to optimise pembrolizumab therapy for dnmMCRC. For simplicity, we assume that pembrolizumab is given at a constant dosage, and the spacing between consecutive pembrolizumab infusions is constant. We also assume that the patient has pembrolizumab at $t = 0$ days, and we consider a treatment regimen lasting for 96 weeks so that the time for the latest allowed infusion is $t = 96$ weeks $= 672$ days. Furthermore, we assume that the patient has a mass of $m = 80$ kg. In our optimisation of pembrolizumab therapy, we consider the following four objectives: tumour volume reduction (TVR), efficacy, efficiency, and toxicity.

We denote $V_{\text{TS}}(\xi_{\text{pembro}}; \eta_{\text{pembro}}, t)$ as the primary tumour volume at time t with treatment with pembrolizumab doses of ξ_{pembro} (in mg/kg) at a dosing interval of η_{pembro} (in weeks), omitting the ξ_{pembro} and η_{pembro} arguments in the case that no treatment is given. We define the TVR from this regimen to be

$$\text{TVR}(\xi_{\text{pembro}}; \eta_{\text{pembro}}, t) := \left(1 - \frac{\int_0^t V_{\text{TS}}(\xi_{\text{pembro}}; \eta_{\text{pembro}}, s)\, ds}{V_{\text{TS}}(0)t}\right) \times 100\%. \tag{4.1}$$

We also define the efficacy similarly as

$$\text{efficacy}(\xi_{\text{pembro}};\eta_{\text{pembro}},t) := \left(1 - \frac{\int_0^t V_{\text{TS}}(\xi_{\text{pembro}};\eta_{\text{pembro}},s)\ ds}{\int_0^t V_{\text{TS}}(s)\ ds}\right) \times 100\%. \tag{4.2}$$

In particular, efficacy represents the extent of tumour volume shrinkage throughout its growth course in comparison to no treatment, i.e the extent of tumour growth inhibition, whereas the TVR reveals how much the tumour volume has reduced since the commencement of treatment. We see that the TVR and efficacy are linearly related, so that an increase in treatment efficacy results in increased TVR, and vice versa, via the formula

$$\text{efficacy}(\xi_{\text{pembro}};\eta_{\text{pembro}},t) = \left(1 - \frac{V_{\text{TS}}(0)t}{\int_0^t V_{\text{TS}}(s)\ ds}\right) \times 100\% + \frac{V_{\text{TS}}(0)t}{\int_0^t V_{\text{TS}}(s)\ ds} \times \text{TVR}\left(\xi_{\text{pembro}};\eta_{\text{pembro}},t\right). \tag{4.3}$$

We can also consider the efficiency of the treatment regimen, with a dosing interval of η_{pembro} weeks and dosage ξ_{pembro} mg/kg given by

$$\text{efficiency}(\xi_{\text{pembro}};\eta_{\text{pembro}},t) := \frac{\text{efficacy}(\xi_{\text{pembro}};\eta_{\text{pembro}},t)}{\xi_{\text{pembro}} m\left(\lfloor \min\left(t,672\right)/7\eta_{\text{pembro}}\rfloor + \theta(672-t)\right)}, \tag{4.4}$$

where $\theta(t)$ is the Heaviside function which equals 1 if $t \geq 0$, and 0 otherwise. In particular, $\xi_{\text{pembro}} m\left(\lfloor \min\left(t,672\right)/7\eta_{\text{pembro}}\rfloor + \theta(672-t)\right)$ is the total dose of pembrolizumab administered by time t, recalling that no treatment is given for $t \geq 672$ days. This corresponds to the ratio between the efficacy and the total dose of pembrolizumab administered.

Finally, we can define the toxicity of the treatment regimen, noting that large enough pembrolizumab concentrations can potentially cause hepatotoxicity and ocular toxicity [76, 77], as well as increase the probability of serious infections and malignancies. Experiments show that dosages of pembrolizumab between 0.1 mg/kg and 10 mg/kg, given every 2 weeks, is safe and tolerable [78, 79]. We thus assume that the threshold for pembrolizumab toxicity is 10 mg/kg every 2 weeks, with higher doses being deemed toxic. To rigorise this notion, we define the toxicity of the treatment regimen, with a dosing interval of η_{pembro} weeks and dosage ξ_{pembro} mg/kg, as

$$\text{toxicity}(\xi_{\text{pembro}};\eta_{\text{pembro}},t) := \max\left(\frac{\max_{s\in[0,t]} A_1(\xi_{\text{pembro}};\eta_{\text{pembro}},s)}{\max_{s\in[0,t]} A_1(10;2,s)}, \frac{\max_{s\in[0,t]} A_1^{\text{LN}}(\xi_{\text{pembro}};\eta_{\text{pembro}},s)}{\max_{s\in[0,t]} A_1^{\text{LN}}(10;2,s)}\right). \tag{4.5}$$

In particular, $A_1(\xi_{\text{pembro}};\eta_{\text{pembro}},s)$ and $A_1^{\text{LN}}(\xi_{\text{pembro}};\eta_{\text{pembro}},s)$ denote the concentrations of A_1 and A_1^{LN} at time s, with pembrolizumab doses of ξ_{pembro} at a dosing interval of η_{pembro}, respectively. In particular, the toxicity quantifies the ratio of the maximum pembrolizumab concentrations from the regimen to those of a 10 mg/kg dose given every 2 weeks, taking the highest value of this ratio between the TDLN and TS. A toxicity greater than 1 indicates a toxic and unsafe regimen, whereas a toxicity of 1 or less signifies a non-toxic and safe regimen, with lower toxicity values corresponding to safer treatments.

Furthermore, we use the two FDA-approved pembrolizumab regimens for the first-line treatment of mMCRC in adults as a benchmark for comparison [80]:

- Treatment 1: 200 mg of pembrolizumab administered by intravenous infusion over a duration of 30 minutes every 3 weeks until disease progression or unacceptable toxicity.
- Treatment 2: 400 mg of pembrolizumab administered by intravenous infusion over a duration of 30 minutes every 6 weeks until disease progression or unacceptable toxicity.

These correspond to the following parameter values in the model:

- Treatment 1: $\xi_j = 200$ mg, $t_j = 21(j-1)$, $n = 32$, $\xi_{\text{pembro}} = 2.5$ mg/kg, $\eta_{\text{pembro}} = 3$ weeks,
- Treatment 2: $\xi_j = 400$ mg, $t_j = 42(j-1)$, $n = 16$, $\xi_{\text{pembro}} = 5$ mg/kg, $\eta_{\text{pembro}} = 6$ weeks.

Denoting the dosing interval of pembrolizumab as η_{pembro}, we perform a sweep across the space $\eta_{\text{pembro}} \in \{1, 2, 3, 4, 6, 8, 12\}$ weeks. These values are integer factors of 96 weeks, and each η_{pembro} corresponds to a distinct number of doses administered. This approach ensures practicality whilst preventing any artefacts that could occur from selecting a treatment regimen that ends at a fixed time of 96 weeks. Taking practicality constraints into account, we consider linearly spaced dosages in the domain $\xi_{\text{pembro}} \in [0.1, 10]$ mg/kg, with a spacing of 0.0125 mg/kg. This corresponds to $\xi_j \in [0.1m, 10m]$ mg $= [8, 800]$ mg with an increment of 1 mg.

We can determine the optimal pembrolizumab therapy by considering the regimen that achieves an acceptable efficacy at 96 weeks whilst maximising treatment efficiency as much as possible and ensuring a toxicity of less than 1. The efficacies of Treatment 1 and Treatment 2 at 96 weeks were calculated to be 62.14%. As such, to ensure that the TVR of the optimal treatment is comparable to current FDA-approved pembrolizumab regimens, we consider threshold efficacies of 62.14%, 62%, 61%, and 60%. We also consider constraints due to practicality, so that ξ_{pembro} is an integer multiple of $0.1m$ mg/kg, corresponding to an integer multiple of 8 mg, leaving the domain for η_{pembro} unchanged. Denoting the space of $(\xi_{\text{pembro}}, \eta_{\text{pembro}})$ pairs that satisfy these criteria as $\mathcal{S}^{\text{prac}}$, the optimal pembrolizumab dosing and spacing, denoted $\xi^{\text{opt}}_{\text{pembro}}$ and $\eta^{\text{opt}}_{\text{pembro}}$, respectively, for a given threshold efficacy $\mathcal{E}_{\text{thresh}}$, satisfy

$$\left(\xi^{\text{opt}}_{\text{pembro}}, \eta^{\text{opt}}_{\text{pembro}}\right) = \underset{\substack{\text{efficacy}(\xi_{\text{pembro}};\eta_{\text{pembro}},672)\geq\mathcal{E}_{\text{thresh}} \\ (\xi_{\text{pembro}},\eta_{\text{pembro}})\in\mathcal{S}^{\text{prac}} \\ \text{toxicity}(\xi_{\text{pembro}};\eta_{\text{pembro}},672)\leq 1}}{\text{argmax}} \text{efficiency}\left(\xi_{\text{pembro}}; \eta_{\text{pembro}}, 672\right). \tag{4.6}$$

Solutions of (4.6) with the previously given threshold efficacies compared to Treatments 1 and 2 are shown in Table 12.

Table 12: Comparison of $\xi^{\text{opt}}_{\text{pembro}}$, dosage, spacing ($\eta^{\text{opt}}_{\text{pembro}}$), TVR, efficacy, efficiency, and toxicity between FDA-approved regimens and optimal treatment regimens for various $\mathscr{E}_{\text{thresh}}$, assuming a patient mass of 80 kg. Tx No. denotes the treatment number, with FDA-approved therapies labelled as Treatments 1 and 2, and optimal regimens labelled as Treatments 3–6.

	Tx Num.	$\mathcal{E}_{\text{thresh}}$ (%)	$\eta^{\text{opt}}_{\text{pembro}}$ (mg/kg)	**Dosage (mg)**	**Spacing (weeks)**	**TVR (%)**	**Efficacy (%)**	**Efficiency (%/mg)**	**Toxicity**
FDA	1	—	—	200	3	34.07	62.14	9.71×10^{-3}	1.83×10^{-1}
	2	—	—	400	6	34.08	62.14	9.71×10^{-3}	2.37×10^{-1}
Optimal	3	62.14	3.3	264	4	34.08	62.14	9.81×10^{-3}	1.98×10^{-1}
	4	62	3.0	240	4	33.87	62.02	1.08×10^{-2}	1.80×10^{-1}
	5	61	1.7	136	4	32.17	61.05	1.87×10^{-2}	1.02×10^{-1}
	6	60	1.2	96	4	30.66	60.18	2.61×10^{-2}	7.21×10^{-2}

Heatmaps of TVR, efficacy, efficiency, and toxicity at $t = 96$ weeks for various η_{pembro} and ξ_{pembro} values are shown in Figure 7. All simulations were done in MATLAB using the dde23 solver with the initial conditions stated in Section 3.

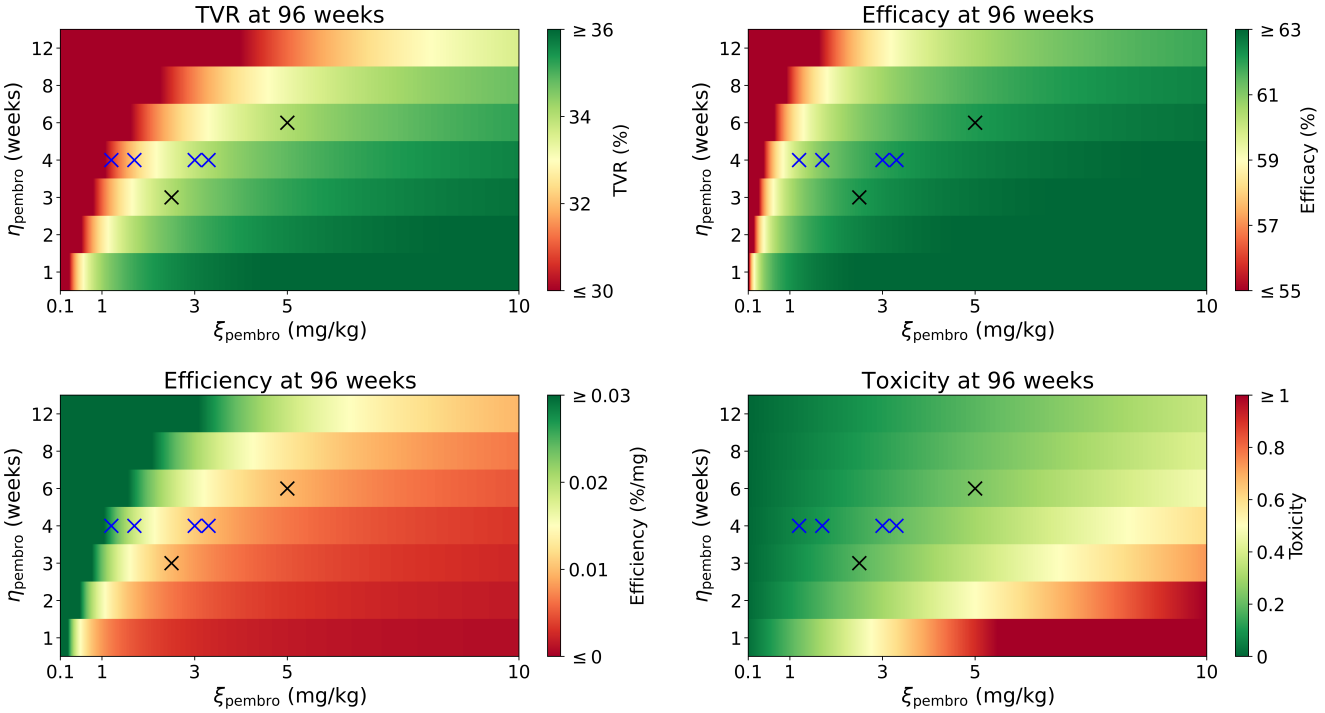

Figure 7: TVR (top left), efficacy (top right), efficiency (bottom left), and toxicity (bottom right) at 96 weeks for $\eta_{\text{pembro}} \in \{1, 2, 3, 4, 6, 8, 12\}$ weeks. We sweep across $\xi_{\text{pembro}} \in [0.1, 10]$ mg/kg with an increment of 0.0125 mg/kg. The FDA-approved regimens (Treatments 1 and 2) for mMCRC are shown in black, and the optimal regimens (Treatments 3–6) are shown in blue.

Time traces of TVR, efficacy, efficiency, and toxicity for Treatments 1–6 are shown in Figure 8.

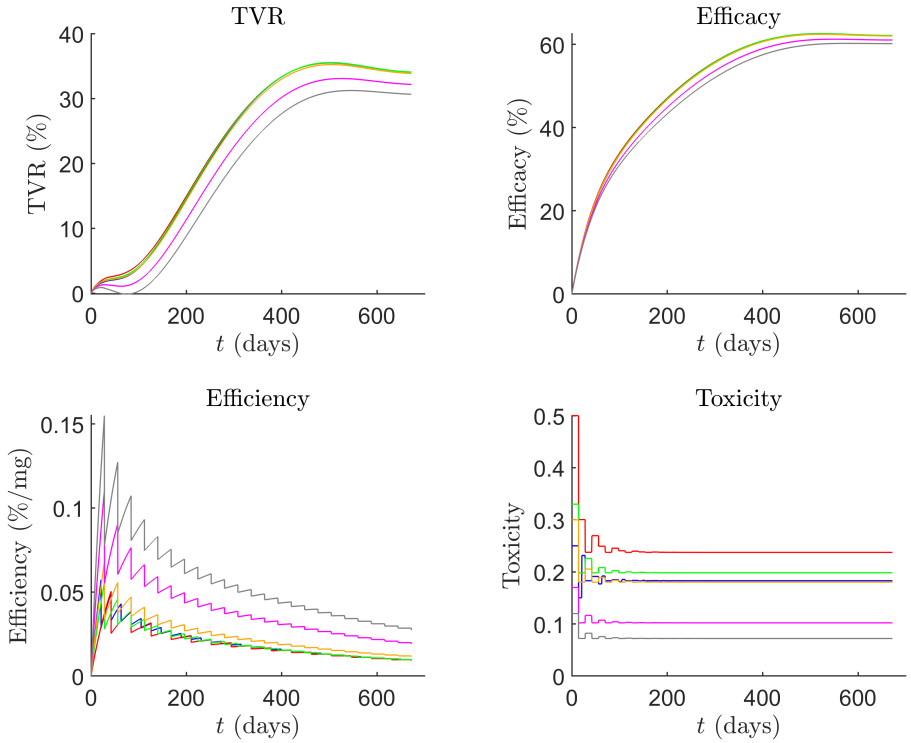

Figure 8: Time traces of TVR (top left), efficacy (top right), efficiency (bottom left), and toxicity (bottom right) for Treatments 1–6 in blue, red, green, orange, magenta, and grey, respectively.

Time traces for the primary tumour volume, V_{TS}, with Treatments 1–6 compared to no treatment are shown in Figure 9.

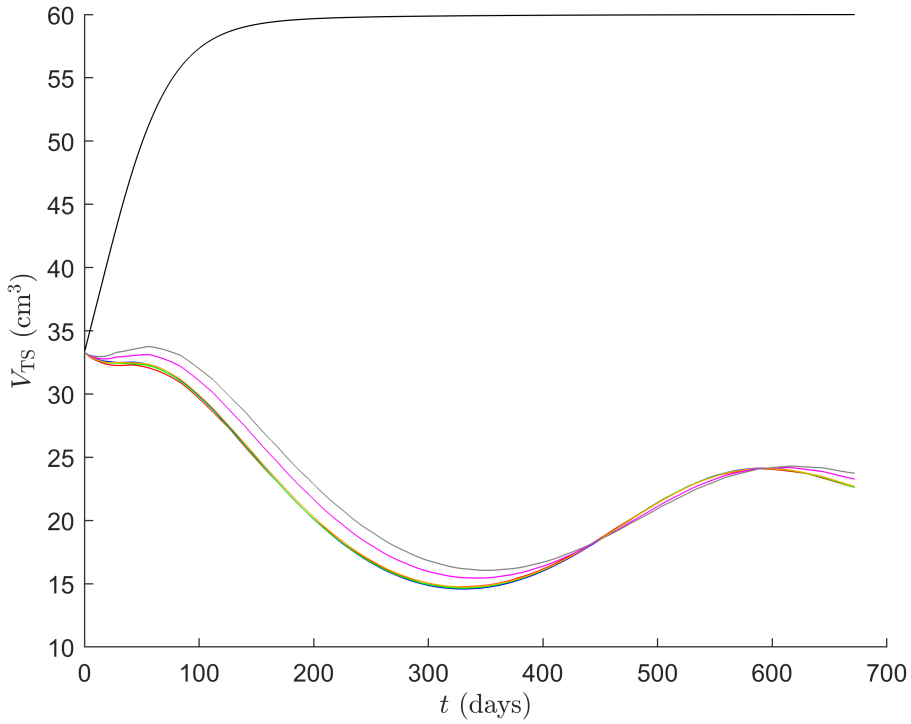

Figure 9: Time traces of V_{TS} up to 96 weeks from commencement, with no treatment in black, and Treatments 1–6 in blue, red, green, orange, magenta, and grey, respectively.

We can also compare the effects of optimal pembrolizumab therapies and FDA-approved regimens to those of no treatment on the TME, with time traces of model variables shown in Figure 10 and average immune cell and cytokine concentrations at 96 weeks shown in Table 13.

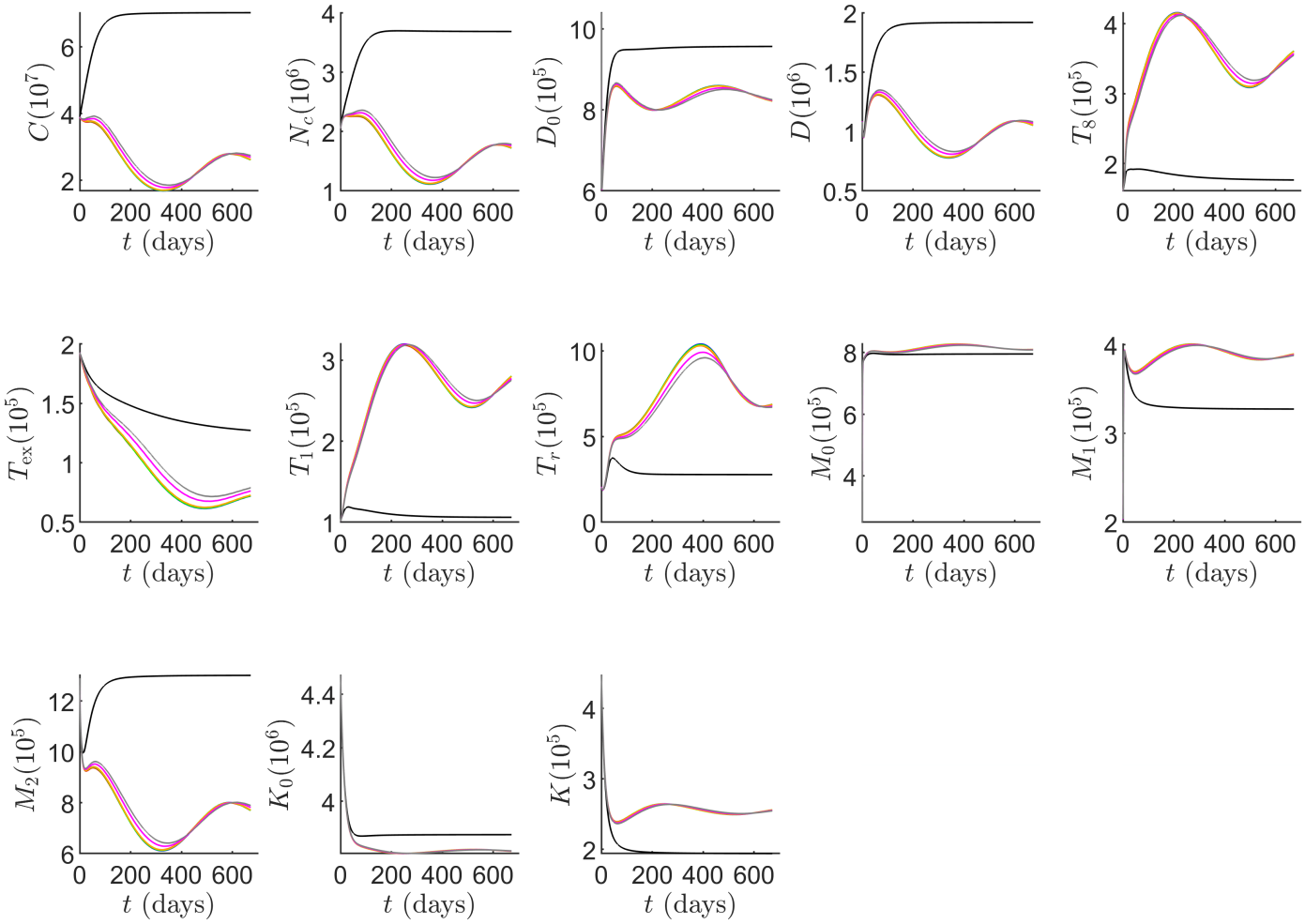

(a) Time traces of cell densities in the TS.

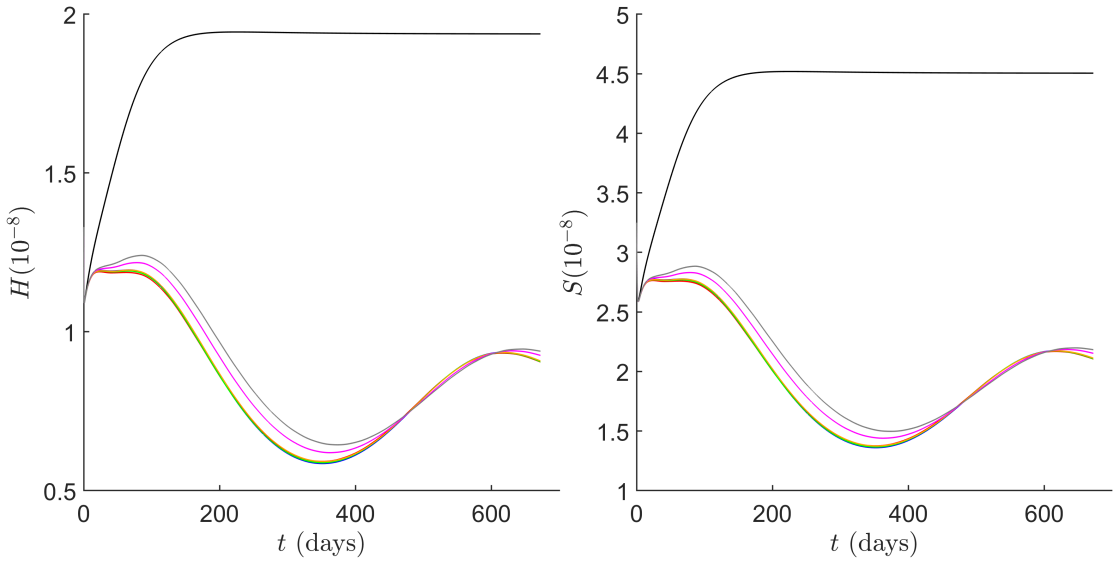

(b) Time traces of DAMP concentrations in the TS.

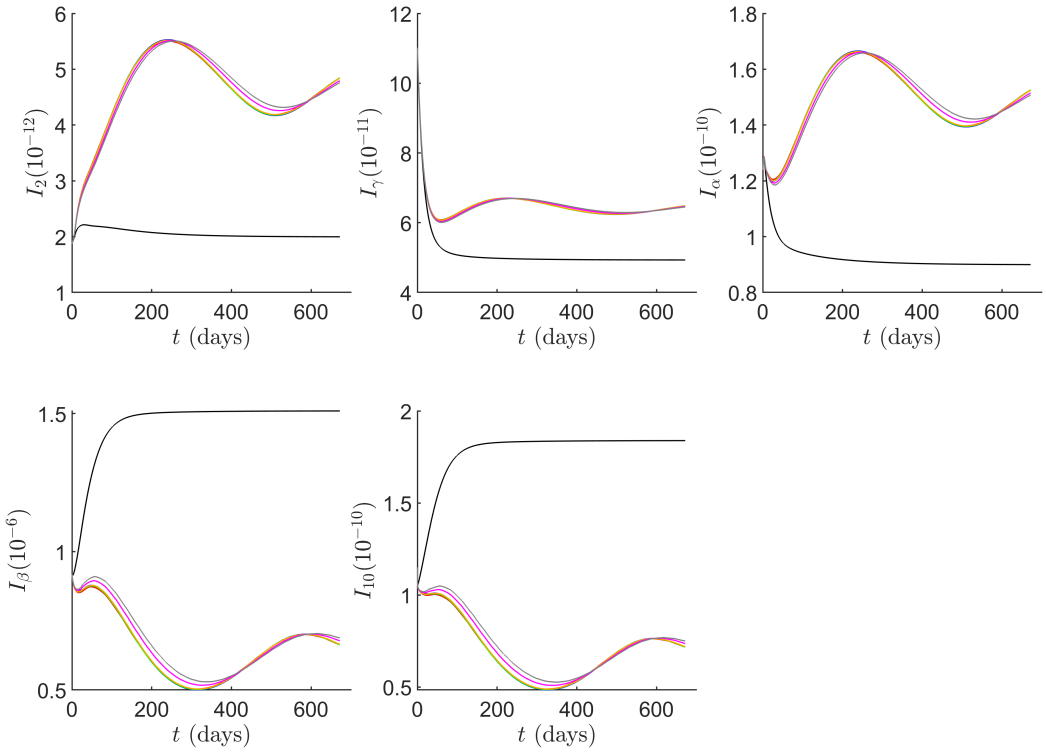

(c) Time traces of cytokine concentrations in the TS.

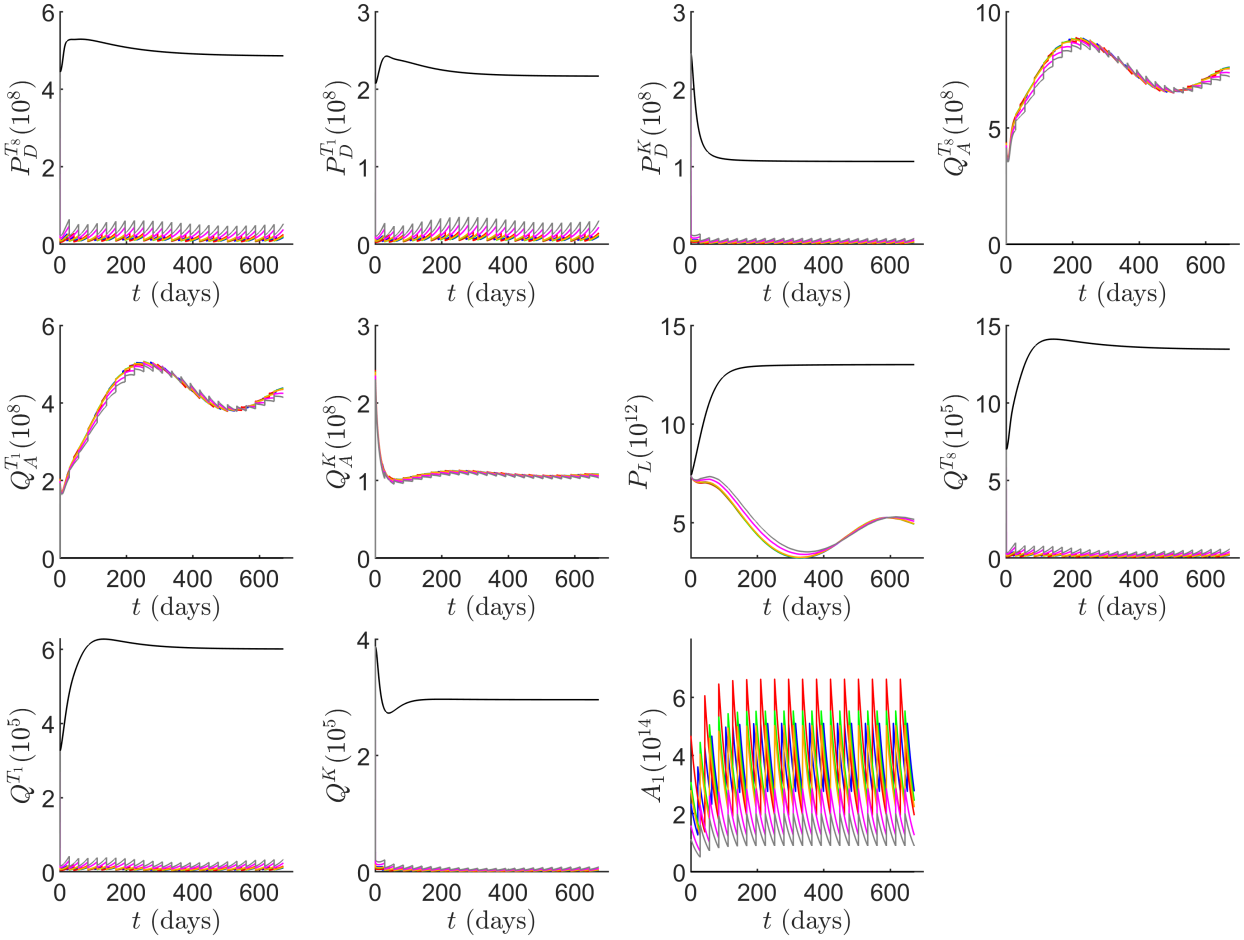

(d) Time traces of pembrolizumab and immune checkpoint-associated concentrations in the TS.

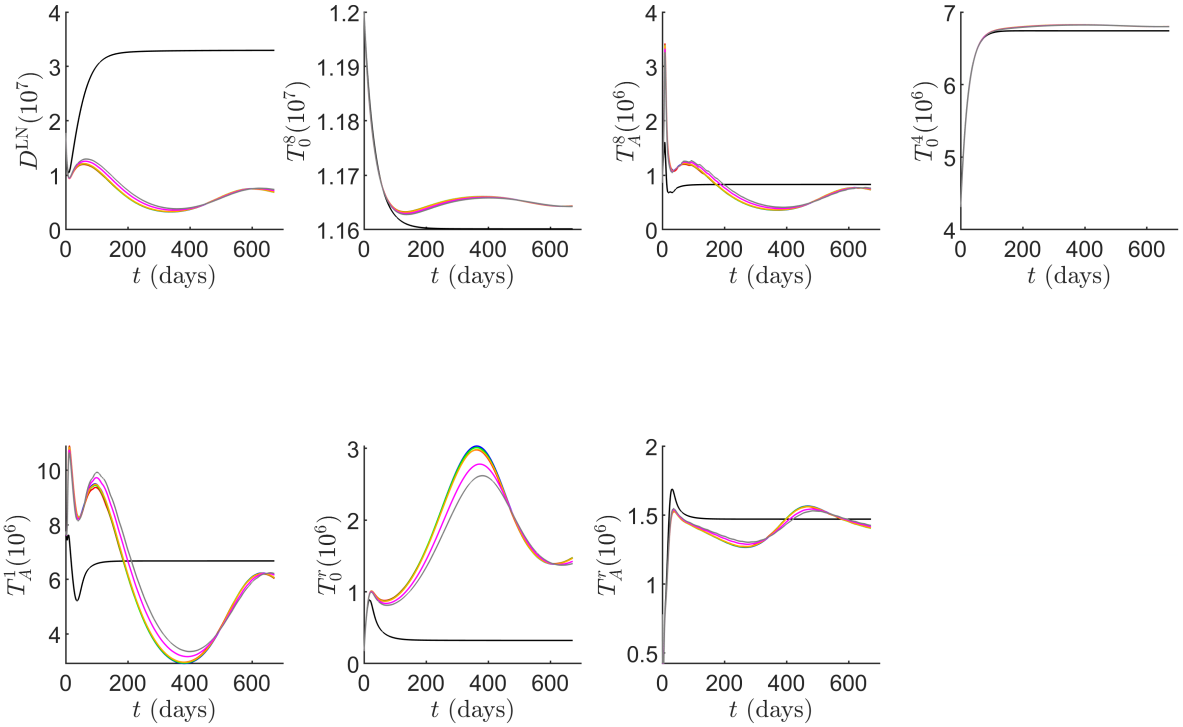

(e) Time traces of cell densities in the TDLN.

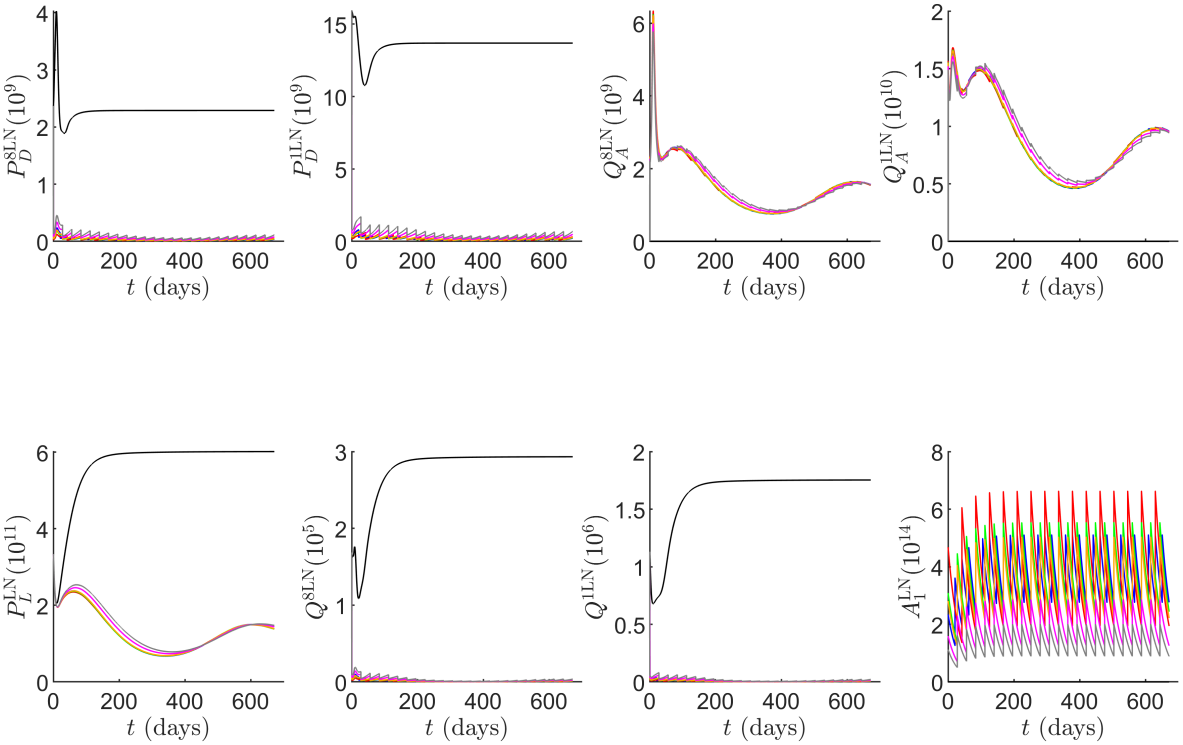

(f) Time traces of pembrolizumab and immune checkpoint-associated concentrations in the TDLN.

Figure 10: Time traces of variables in the model, with the units of the variables as in Table 1. Time traces with no treatment are in black, and Treatments 1–6 in blue, red, green, orange, magenta, and grey, respectively.

Table 13: Comparison of average immune cell and cytokine concentrations at 96 weeks between no treatment and Treatments 1–6. Units of variables are as in Table 1.

	No Tx	**Treatment 1**	**Treatment 2**	**Treatment 3**	**Treatment 4**	**Treatment 5**	**Treatment 6**
$\boldsymbol{C}$	6.79×10^{7}	2.54×10^{7}	2.54×10^{7}	2.54×10^{7}	2.55×10^{7}	2.62×10^{7}	2.67×10^{7}
$\boldsymbol{N_c}$	3.57×10^{6}	1.63×10^{6}	1.63×10^{6}	1.63×10^{6}	1.64×10^{6}	1.68×10^{6}	1.71×10^{6}
$\boldsymbol{H}$	1.88×10^{-8}	8.58×10^{-9}	8.59×10^{-9}	8.58×10^{-9}	8.61×10^{-9}	8.83×10^{-9}	9.02×10^{-9}
$\boldsymbol{S}$	4.36×10^{-8}	2.00×10^{-8}	2.00×10^{-8}	2.00×10^{-8}	2.00×10^{-8}	2.05×10^{-8}	2.10×10^{-8}
$\boldsymbol{D_0}$	9.43×10^{5}	8.29×10^{5}	8.29×10^{5}	8.29×10^{5}	8.29×10^{5}	8.28×10^{5}	8.27×10^{5}
$\boldsymbol{D}$	1.86×10^{6}	1.01×10^{6}	1.01×10^{6}	1.01×10^{6}	1.01×10^{6}	1.03×10^{6}	1.04×10^{6}
$\boldsymbol{D^{\mathrm{LN}}}$	3.10×10^{7}	6.64×10^{6}	6.63×10^{6}	6.63×10^{6}	6.67×10^{6}	6.94×10^{6}	7.19×10^{6}
$\boldsymbol{T_0^8}$	1.16×10^{7}	1.17×10^{7}	1.17×10^{7}	1.17×10^{7}	1.17×10^{7}	1.17×10^{7}	1.17×10^{7}
$\boldsymbol{T_A^8}$	8.31×10^{5}	7.23×10^{5}	7.23×10^{5}	7.23×10^{5}	7.26×10^{5}	7.46×10^{5}	7.63×10^{5}
$\boldsymbol{T_8}$	1.82×10^{5}	3.48×10^{5}	3.48×10^{5}	3.48×10^{5}	3.48×10^{5}	3.48×10^{5}	3.49×10^{5}
$\boldsymbol{T_{\mathrm{ex}}}$	1.43×10^{5}	9.55×10^{4}	9.57×10^{4}	9.56×10^{4}	9.64×10^{4}	1.02×10^{5}	1.06×10^{5}
$\boldsymbol{T_0^4}$	6.66×10^{6}	6.71×10^{6}	6.71×10^{6}	6.71×10^{6}	6.71×10^{6}	6.71×10^{6}	6.71×10^{6}
$\boldsymbol{T_A^1}$	6.61×10^{6}	5.65×10^{6}	5.65×10^{6}	5.65×10^{6}	5.67×10^{6}	5.84×10^{6}	5.98×10^{6}
$\boldsymbol{T_1}$	1.09×10^{5}	2.61×10^{5}	2.61×10^{5}	2.61×10^{5}	2.61×10^{5}	2.62×10^{5}	2.62×10^{5}
$\boldsymbol{T_0^r}$	3.56×10^{5}	1.81×10^{6}	1.80×10^{6}	1.80×10^{6}	1.79×10^{6}	1.71×10^{6}	1.65×10^{6}
$\boldsymbol{T_A^r}$	1.46×10^{6}	1.40×10^{6}	1.40×10^{6}	1.40×10^{6}	1.40×10^{6}	1.40×10^{6}	1.41×10^{6}
$\boldsymbol{T_r}$	2.85×10^{5}	7.48×10^{5}	7.46×10^{5}	7.47×10^{5}	7.45×10^{5}	7.26×10^{5}	7.10×10^{5}
$\boldsymbol{M_0}$	7.93×10^{5}	8.13×10^{5}	8.13×10^{5}	8.13×10^{5}	8.12×10^{5}	8.11×10^{5}	8.10×10^{5}
$\boldsymbol{M_1}$	3.31×10^{5}	3.88×10^{5}	3.88×10^{5}	3.88×10^{5}	3.88×10^{5}	3.88×10^{5}	3.87×10^{5}
$\boldsymbol{M_2}$	1.27×10^{6}	7.58×10^{5}	7.58×10^{5}	7.58×10^{5}	7.59×10^{5}	7.68×10^{5}	7.77×10^{5}
$\boldsymbol{K_0}$	3.89×10^{6}	3.83×10^{6}	3.83×10^{6}	3.83×10^{6}	3.83×10^{6}	3.83×10^{6}	3.83×10^{6}
$\boldsymbol{K}$	2.02×10^{5}	2.57×10^{5}	2.57×10^{5}	2.57×10^{5}	2.57×10^{5}	2.57×10^{5}	2.57×10^{5}
$\boldsymbol{I_2}$	2.05×10^{-12}	4.56×10^{-12}	4.56×10^{-12}	4.56×10^{-12}	4.56×10^{-12}	4.57×10^{-12}	4.58×10^{-12}
$\boldsymbol{I_\gamma}$	5.12×10^{-11}	6.48×10^{-11}	6.48×10^{-11}	6.48×10^{-11}	6.48×10^{-11}	6.48×10^{-11}	6.49×10^{-11}
$\boldsymbol{I_\alpha}$	9.25×10^{-11}	1.48×10^{-10}	1.48×10^{-10}	1.48×10^{-10}	1.48×10^{-10}	1.48×10^{-10}	1.48×10^{-10}
$\boldsymbol{I_\beta}$	1.46×10^{-6}	6.55×10^{-7}	6.55×10^{-7}	6.55×10^{-7}	6.56×10^{-7}	6.68×10^{-7}	6.78×10^{-7}
$\boldsymbol{I_{10}}$	1.78×10^{-10}	7.00×10^{-11}	7.00×10^{-11}	7.00×10^{-11}	7.02×10^{-11}	7.19×10^{-11}	7.33×10^{-11}

5 Discussion

We proceed to analyse the results from Figure 7, Figure 8, Figure 9, Figure 10, and Table 13 will be discussed in detail, and compare them to findings from laMCRC reported in [36]. We first analyse Figure 9, Figure 10, and Table 13 for the FDA-approved treatment regimens, Treatment 1 and Treatment 2.

We can see from Figure 9 that the FDA-approved treatments are effective during the first half of the treatment period at eradicating cancer cells, with the primary tumour volume reaching a minimum of approximately 14.59 cm^3 at 330 days. This corresponds to a 56.1% decrease from the initial volume and a 75.6% reduction compared to the tumour volume without treatment at that time. We note that it takes a couple of months of pembrolizumab therapy for consistent tumour reductions to be observed, in agreement with experimental findings for mMCRC [11]. However, the treatment becomes insufficiently effective thereafter, leading to an increase in V_{TS}, which peaks at 24.14 cm^3 at 591 days before beginning to decline again, albeit at a slower rate. This is in contrast to the case of laMCRC, where treatment leads to a rapid and sustained decrease in total cancer concentration, and equivalently the tumour volume, even after treatment ends at 12 weeks, with a reduction of more than 85% by 18 weeks.

To justify this behaviour, we first examine the time traces of the model components shown in Figure 10, which allow us to identify key factors that contribute to maximising cancer reduction. One immediate point of note is that the TME is significantly more immunogenic and pro-inflammatory in laMCRC, with the initial concentrations of pro-inflammatory effector CD8+ T cells, effector Th1 cells, activated NK cells and M1 macrophages being 2.43×10^5 cell/cm^3, 1.04×10^5 cell/cm^3, 5.20×10^6 cell/cm^3, and 6.61×10^5 cell/cm^3, respectively, compared to 1.61×10^5 cell/cm^3, 1.01×10^5 cell/cm^3, 4.47×10^5 cell/cm^3, and 2.09×10^5 cell/cm^3 in dnmMCRC. Similarly, the concentrations of anti-inflammatory cells, particularly viable cancer cells, effector Tregs, and M2 macrophages, are initially 1.79×10^5 cell/cm^3, 2.12×10^5 cell/cm^3, and 1.23×10^6 cell/cm^3 in laMCRC, respectively, compared to the generally larger values of 3.90×10^7 cell/cm^3, 2.02×10^5 cell/cm^3, and 1.29×10^6 cell/cm^3 in dnmMCRC. As such, in dnmMCRC, the TME is so strongly anti-inflammatory that a greater degree of stimulation is required to shift the system toward the more pro-inflammatory state as observed in laMCRC, with this transition inherently requiring more time.

Another important observation is that pembrolizumab therapy leads to a substantial increase in the concentration of activated and effector pro-inflammatory immune cells within the TS, compared to without treatment. Specifically, the concentrations of effector CD8+ T cells and effector Th1 cells increase significantly and monotonically, reaching peak values of 4.16×10^5 cell/cm^3 and 3.20×10^5 cell/cm^3 at 214 and 251 days, respectively, compared to 1.84×10^5 cell/cm^3 and 1.08×10^5 cell/cm^3 without treatment. Similarly, after an initial transient decrease, the concentrations of pro-inflammatory activated NK cells and M1 macrophages increase, reaching peaks of 2.64×10^5 cell/cm^3 and 4.01×10^5 cell/cm^3, respectively, at 245 and 269 days. This trend is reflected in the concentrations of pro-inflammatory cytokines IL-2, IFN-γ, and TNF which, after transient decreases, rise to 5.53×10^{-12} molec/cm^3, 6.71×10^{-11} molec/cm^3, and 1.67×10^{-10} molec/cm^3 by 241, 224, and 239 days, respectively, compared to 2.05×10^{-12} molec/cm^3, 4.97×10^{-11} molec/cm^3 and 9.13×10^{-11} molec/cm^3 in the absence of therapy. However, following their peaks, all these concentrations decline markedly. The concentrations of effector CD8+ T cells, effector Th1 cells, activated NK cells, M1 macrophages, IL-2, IFN-γ, and TNF reach their minimum values at approximately 498, 515, 525, 537, 510, 496, and 510 days, respectively, with corresponding concentrations of 3.09×10^5 cell/cm^3, 2.42×10^5 cell/cm^3, 2.49×10^5 cell/cm^3, 3.83×10^5 cell/cm^3, 4.17×10^{-12} molec/cm^3, 6.24×10^{-11} molec/cm^3, and 1.39×10^{-10} molec/cm^3, before beginning to increase again. Nonetheless, the concentration of pro-inflammatory cells and cytokines in the TS remains significantly higher than without treatment, with the average concentrations of effector CD8+ T cells, effector Th1 cells, activated NK cells, M1 macrophages, IL-2, IFN-γ, and TNF under treatment being 3.48×10^5 cell/cm^3, 2.61×10^5 cell/cm^3, 2.57×10^5 cell/cm^3, 3.88×10^5 cell/cm^3, 4.56×10^{-12} molec/cm^3, 6.48×10^{-11} molec/cm^3, and 1.48×10^{-10} molec/cm^3, respectively, all notably higher than their counterparts without treatment, which are 1.82×10^5 cell/cm^3, 1.09×10^5 cell/cm^3, 2.02×10^5 cell/cm^3, 3.31×10^5 cell/cm^3, 2.05×10^{-12} molec/cm^3, 5.12×10^{-11} molec/cm^3, and 9.25×10^{-11} molec/cm^3, without, using data from Table 13.

This behaviour is mirrored in the anti-inflammatory cells and cytokines within the TS, including viable cancer cells, M2 macrophages, TGF-β, and IL-10, whose concentrations decrease significantly up to approximately 329, 324, 317, and 327 days under treatment, respectively, reaching values of 1.68×10^7 cell/cm^3, 6.11×10^5 cell/cm^3, 5.00×10^{-7} molec/cm^3, and 4.84×10^{-11} molec/cm^3—compared to 7.01×10^7 cell/cm^3, 1.30×10^6 cell/cm^3, 1.51×10^{-6} molec/cm^3, and 1.84×10^{-10} molec/cm^3 without treatment. Following this decline, their concentrations rise again, peaking at around 589 days with corresponding concentrations of 2.80×10^7 cell/cm^3, 8.01×10^5 cell/cm^3, 7.02×10^{-7} molec/cm^3, and 7.64×10^{-11} molec/cm^3, before decreasing once more. Nonetheless, the concentrations of these

components remains significantly lower than without treatment, with the average concentrations of viable cancer cells, M2 macrophages, TGF-β, and IL-10 under treatment being 2.54×10^7 cell/cm^3, 7.58×10^5 cell/cm^3, 6.55×10^{-7} molec/cm^3, and 7.00×10^{-11} molec/cm^3, respectively, which are all lower than their counterparts without treatment, which are 6.79×10^7 cell/cm^3, 1.27×10^6 cell/cm^3, 1.46×10^{-6} molec/cm^3, and 1.78×10^{-10} molec/cm^3, using data from Table 13.

These oscillations in concentration are perpetuated by several positive feedback loops within the TME. Firstly, increases in effector CD8+ and Th1 cell concentration lead to an increased concentration of IL-2, a key growth factor for these cells and an activator of naive NK cells. This, in turn, enhances IL-2 production, further stimulating effector CD8+ and Th1 cell proliferation, reinforcing the loop. Furthermore, elevated levels of pro-inflammatory cells enhance tumour cell lysis and increase production of pro-inflammatory cytokines, such as TNF and IFN-γ, which drive cancer cell necrosis and macrophage polarisation into the pro-inflammatory M1 phenotype, resulting in another positive feedback loop. Moreover, decreased concentrations of anti-inflammatory cells lead to diminished production of anti-inflammatory cytokines, which decreases polarisation of macrophages to the M2 phenotype, further decreasing anti-inflammatory cytokine production and reinforcing a positive feedback loop. A particularly potent example of this occurs with respect to TGF-β: as the levels of anti-inflammatory cells decline, TGF-β concentrations decrease, which reduces the inhibition of cancer cell lysis by effector CD8+ T cells and activated NK cells, diminishes suppression of NK cell activation, and reduces M2 macrophage polarisation. This further lowers the number of immunosuppressive cells, which perpetuates the decline in TGF-β concentration and amplifies the anti-tumour response. Furthermore, another important positive feedback loop involves PD-L1 concentrations in the TS. As anti-inflammatory cell concentrations, in particular viable cancer cells and M2 macrophages, decrease, there is a decrease in the total PD-L1 concentration in the TS, resulting in reduced PD-1/PD-L1 complex formation, and enhanced lysis of cancer cells by effector CD8+ T cells and activated NK cells. This further lowers cancer cell concentrations and, consequently, PD-L1 concentration. However, these feedback mechanisms are bidirectional: a decline in pro-inflammatory cell concentrations leads to reduced levels of pro-inflammatory cytokines, and vice versa. Similarly, increases in anti-inflammatory cell concentrations promote greater production of anti-inflammatory cytokines, and vice versa.

We now aim to provide an explanation for the sudden change in dynamics observed, focusing on three key aspects: DC maturation and migration to the TDLN, T cell proliferation and activation within the TDLN, and Treg hyperproliferation at the TS. Up to 330 days, as treatment progresses, tumour burden decreases, resulting in a decrease in the magnitude of necrotic cancer cells and, consequently, lower DAMP release and reduced DC maturation. This leads to a substantial decline in the concentration of mature DCs, reaching minima of 7.78×10^5 cell/cm^3 and 3.25×10^6 cell/cm^3 in the TS and TDLN, respectively, compared to 1.92×10^6 cell/cm^3 and 3.29×10^7 cell/cm^3 without treatment at the same time point. However, the concentration of mature DCs peaks to 1.09×10^6 cell/cm^3 in the TS and 7.52×10^6 cell/cm^3 in the TDLN at approximately 600 days, before declining again, closely mirroring the behaviour of anti-inflammatory cell populations.

Decreased DCs in the TDLN lead to decreased activation and proliferation of T cells in the TDLN; however, this is not the only contributing factor. Another important factor is the concentration of effector Tregs in the TDLN, which directly inhibits T cell proliferation and activation. Although their concentration initially decreases compared to without treatment, the reduction is insufficient to relieve this inhibition. Specifically, the effector Treg population in the TDLN exhibits a pattern similar to other anti-inflammatory cells, showing a pronounced dip to 1.27×10^6 cell/cm^3 at 268 days, followed by a peak of 1.57×10^6 cell/cm^3 at 468 days, before declining again, compared to a steady-state value

of 1.47×10^6 cell/cm^3 without treatment. This, in conjunction with the decreased concentration of mature DCs in the TDLN, explains why the concentrations of effector CD8+ T cells and effector Th1 cells, after an initial transient phase, peak at 73 and 94 days, respectively, with concentrations reaching 1.22×10^6 cell/cm^3 and 9.50×10^6 cell/cm^3. These concentrations then fall to their minimum at 371 and 382 days, respectively, with values of 3.56×10^5 cell/cm^3 and 2.92×10^6 cell/cm^3, respectively. Notably, after 173 and 186 days, respectively, the concentrations of these effector cells become less than without treatment, leading to reduced cancer cell killing and decreased concentrations of pro-inflammatory cells in the TS. This initiates a cascade of effects that contribute to the later observed change in dynamics at 330 days, triggering the feedback loops described earlier.

This leads into the final critical aspect, which causes the treatment to fail: the extensive hyperproliferation of effector Tregs in the TS as a consequence of prolonged treatment. This population swells to a peak concentration of 1.04×10^6 cell/cm^3 at 391 days, far exceeding the value of 2.78×10^5 cell/cm^3 observed without treatment, before subsequently declining. This 3.74-fold increase results in strong inhibition of IL-2-mediated pro-inflammatory T cell growth, reduced IFN-γ production by T cells, and increased secretion of TGF-β, thereby exacerbating the previously mentioned TGF-β-driven feedback loop. Clinically, similar phenomena have been observed in cases of hyperprogressive disease following ICI therapy [81] and could represent a potential mechanism of acquired resistance to ICI therapy [82], both of which have been associated with treatment failure. However, given the significantly elevated effector CD8+ T cell and Th1 cell populations observed in the TS following immunotherapy, the hyperproliferation of Tregs is not entirely unexpected. A key distinction between this phenomenon in laMCRC and dnmMCRC is that Tregs may act as a regulatory mechanism to prevent excessive immune activation once the tumour burden is sufficiently reduced. Nevertheless, in dnmMCRC, this regulatory mechanism is triggered prematurely, resulting in a dampened immune response that ultimately fails to achieve complete cancer eradication.

This motivates the introduction of an additional immunotherapeutic agent aimed at depleting Tregs—an objective fulfilled by anti-CTLA-4 antibodies, which target the CTLA-4 immune checkpoint. A successful example of this approach is seen in the extended CheckMate 142 study, which evaluated the efficacy of combination treatment with nivolumab, a fully human IgG4 PD-1 antibody, and ipilimumab, a CTLA-4 antibody, for pretreated mMCRC [83]. In this study, nivolumab was administered at 3 mg/kg every three weeks, while ipilimumab was given at 1 mg/kg every three weeks for the first four doses, followed by maintenance therapy with nivolumab (3 mg/kg) every two weeks. Tumour burden reduction from baseline was observed in 77% of patients, and the 9-month and 12-month overall survival rates were 87% (95% CI 80.0–92.2%) and 85% (95% CI 77.0—90.2%), respectively [84]. These results prompted the FDA to approve combination nivolumab and ipilimumab therapy for pretreated mMCRC on July 10, 2018.

However, ipilimumab is not the only anti-CTLA-4 antibody, with promising results being reported from a phase I trial evaluating botensilimab, a fragment crystallisable (Fc)-enhanced anti-CTLA-4 antibody, with and without balstilimab, a fully human PD-1 antibody, in metastatic relapsed/refractory MSS CRC [85]. In particular, botensilimab has been demonstrated to be more potent in depleting Tregs than ipilimumab [86], largely due to enhanced antibody-dependent cellular cytotoxicity and phagocytosis mechanisms. The optimal timing, dosage, and scheduling of combination PD-1 and CTLA-4 inhibitor therapies remain important areas for future investigation. It is important to note, however, that prolonged use of anti-CTLA-4 antibodies carries a risk of autoimmune and immune-related adverse events [87], which must be carefully balanced against therapeutic benefit.

Another key observation is the substantial decrease in exhausted CD8+ T cells with pembrolizumab treatment. The average concentration of exhausted CD8+ T cells across the treatment period is 9.56×10^4 cell/cm^3, which is more than 33% lower than the 1.43×10^5 cell/cm^3 observed without treatment. We thus see that the concentration of exhausted CD8+ T cells plays a major role in treatment efficacy, as reducing the population of exhausted T cells leads to an increased concentration of effector cytotoxic CD8+ T cells, thereby enhancing cancer cell eradication.

We can also analyse the impact of therapy on the concentration of PD-1, PD-1/PD-L1, and PD-1/PD-L1 complex in the TS and the TDLN. As expected, pembrolizumab therapy significantly reduces the concentration of unbound PD-1 receptors on PD-1-expressing cells in both the TS and TDLN, with reductions of approximately 97.7% at trough and 98.7% at peak, very similar to results observed in laMCRC. Additionally, the concentration of PD-1/PD-L1 complexes on cells in the TS and TDLN decreases by more than 99% throughout treatment, as nearly all PD-1 receptors become bound by pembrolizumab, forming PD-1/pembrolizumab complexes. Consequently, there is enhanced lysis of cancer cells by effector CD8+ T cells and activated NK cells, reduced inhibition of pro-inflammatory T cell proliferation and activation, and a decrease in the number of activated and effector Tregs. Thus, we see that the extent of PD-1 receptor engagement and reduction in PD-1/PD-L1 complex concentration are critical factors in influencing treatment efficacy and success.

It is also beneficial for us to compare and analyse the time traces of TVR, efficacy, efficiency, and toxicity of Treatments 1–6 as shown in Figure 8. As expected, the TVRs and efficacies of Treatments 1 and 2 are similar to those of Treatments 3–4 throughout the treatment period, with efficacy being a monotonically increasing function of time. We note that the TVRs and efficacies of Treatments 5 and 6 are slightly lower than those of the other treatments. However, it is important to note that PD-1 receptor engagement by pembrolizumab saturates at relatively low doses, with the KEYNOTE-001 study demonstrating that 2 mg/kg of pembrolizumab is sufficient to saturate unbound PD-1 receptors and achieve maximal anti-tumour activity [88]. Therefore, despite the lower dosages and extended dosing intervals of the optimal regimens, the optimal treatments are significantly more efficient than Treatments 1 and 2, while maintaining comparable efficacy. As a result, the optimal dosing regimens are more efficient and exhibit lower overall dosing than the FDA-approved regimens while still achieving comparable efficacy and TVR. Finally, as expected, the toxicity of all treatments is generally a non-increasing function of time; however, if pembrolizumab concentrations are sufficiently high, small spikes in toxicity may occur following dose administration.

We now shift our focus to Figure 7. We see that TVR increases as the dosing increases and spacing decreases, though with diminishing returns at higher doses or shorter intervals. In particular, the TVRs and efficacies of all optimal regimens are high, with minimal deviations near these regions.

In the spirit of completeness, we verify that Treatments 1 and 2, the FDA-approved regimens, are non-toxic and compare their toxicity to that of the optimal regimens found. As expected, Treatments 1 and 2 are non-toxic, with toxicities of 1.83×10^{-1} and 2.37×10^{-1}, respectively, whilst the optimal regimens have lower or comparable toxicity. Treatments 5 and 6, consisting of 136 mg and 96 mg of pembrolizumab administered every four weeks, are of particular interest, as they achieve comparable TVR and efficacy to Treatments 1 and 2 while being significantly less toxic, making them potentially better options for vulnerable patient populations.

Unsurprisingly, the FDA-approved treatments are very efficient, with the efficiency of Treatment 1 and 2 being approximately 9.71×10^{-3}%/mg by 96 weeks. However, these pale in comparison to the

other optimal regimens, particularly Treatment 6, which has an efficiency of $2.61 \times 10^{-2}\%/\text{mg}$ — more than twice that of Treatments 1 and 2. There is also a clear transition between efficient and inefficient treatments, marked by the rapid shift in efficiency as one deviates from local optima. A treatment is inefficient if its TVR is low, regardless of the dosing and spacing (corresponding to the top left inefficient region in Figure 7), or if an excessive amount of pembrolizumab is administered, regardless of the TVR (corresponding to the bottom right inefficient region in Figure 7).

Striking a balance between TVR, efficiency, and toxicity is challenging, and the current FDA-approved regimens for mMCRC achieve this balance reasonably well. Nonetheless, the optimal regimens defined by Treatments 3–6 in Table 12 are more efficient, lead to comparable TVR, and are more cost-effective and convenient than current regimens, all while maintaining practicality and safety.

It should be noted that the model has several limitations, many of which exist for simplicity, but addressing these issues offers exciting avenues for future research.

- We ignored spatial effects in the model, however, their resolution can provide information about the distribution and clustering of different immune cell types in the TME and their clinical implications [89, 90].
- We assumed that the death rates were constant throughout the T cell proliferation program; however, linear death rates were shown to markedly improve the quality of fit of Deenick et al.'s model [91] to experimental data [92].
- We considered only the M1/M2 macrophage dichotomy, however, their plasticity motivates the description of their phenotypes as a continuum, giving them the ability to adapt their functions to achieve mixtures of M1/M2 responses and functions [49].
- In the optimisation of pembrolizumab therapy, we restricted ourselves to treatments with constant dosing and spacing as is common in the literature; however, varying dosages and dosing frequencies may result in improved regimens.
- We did not consider T cell avidity, the overall strength of a TCR-pMHC interaction, which governs whether a cancer cell will be successfully killed [93]. In particular, high-avidity T cells are necessary for lysing cancer cells and durable tumour eradication, while low-avidity T cells are ineffective and may inhibit high-avidity T cells [94, 95].
- We also did not consider the influence of cytokines in the TDLN for T cell activation and proliferation, which are important in influencing effector T cell differentiation [96, 97].
- The definition of toxicity does not account for its potential origins in autoimmunity, which is a crucial component of certain adverse effects [76].
- The model does not explicitly account for additional anatomical compartments such as the spleen, nor does it directly model metastasis, which may impact the accuracy of systemic immune dynamics and tumour-specific responses.
- The dnmMCRC model does not apply in many cases of recurrent mMCRC, as these cases often lack a primary tumour.

In this work, we have extended Hawi et al.'s model to mathematically model many immune cell types in the TME of dnmMCRC, using experimental data to govern parameter estimation, and finally

analysing and optimising pembrolizumab therapy for TVR, efficiency, and toxicity. We conclude that, although pembrolizumab monotherapy leads to partial clinical response, it is insufficient for complete tumour eradication in dnmMCRC, highlighting the need for additional therapeutic agents such as anti-CTLA-4 antibodies for Treg depletion. This is in contrast to laMCRC, where pembrolizumab monotherapy is sufficient. Furthermore, we demonstrate that administering low to medium doses of pembrolizumab every four weeks achieves comparable efficacy to FDA-approved regimens while offering reduced toxicity and improved treatment efficiency. Overall, this work lays the foundation for deeper insights into tumour-immune dynamics and offers a flexible framework that can be expanded to advance cancer research and improve therapeutic outcomes.

6 CRediT authorship contribution statement

Georgio Hawi: conceptualisation, data curation, formal analysis, funding acquisition, investigation, methodology, project administration, resources, software, validation, visualisation, writing — original draft, writing — review & editing.
Peter S. Kim: conceptualisation, formal analysis, funding acquisition, investigation, methodology, project administration, resources, supervision, validation, visualisation, writing — original draft, writing — review & editing.
Peter P. Lee: conceptualisation, formal analysis, investigation, methodology, project administration, resources, supervision, validation, visualisation, writing — original draft, writing — review & editing.

7 Declaration of Competing Interests

The authors declare that they have no known competing financial interests or personal relationships that could have appeared to influence the work reported in this paper.

8 Data availability

All data and procedures are available within the manuscript and its Supporting Information file.

9 Acknowledgements

This work was supported by an Australian Government Research Training Program Scholarship. PSK gratefully acknowledges support from the Australian Research Council Discovery Project (DP230100485).

References

[1] Biller LH, Schrag D. Diagnosis and Treatment of Metastatic Colorectal Cancer: A Review. JAMA. 2021 Feb;325(7):669. Available from: https://doi.org/10.1001/jama.2021.0106.

[2] Cook AD, Single R, McCahill LE. Surgical Resection of Primary Tumors in Patients Who Present With Stage IV Colorectal Cancer: An Analysis of Surveillance, Epidemiology, and End Results Data, 1988 to 2000. Annals of Surgical Oncology. 2005 Jun;12(8):637–645. Available from: https://doi.org/10.1245/ASO.2005.06.012.

[3] Andrew AS, Parker S, Anderson JC, Rees JR, Robinson C, Riddle B, et al. Risk Factors for Diagnosis of Colorectal Cancer at a Late Stage: a Population-Based Study. Journal of General Internal Medicine. 2018 Oct;33(12):2100–2105. Available from: https://doi.org/10.1007/s11606-018-4648-7.

[4] Rawla P, Sunkara T, Barsouk A. Epidemiology of colorectal cancer: incidence, mortality, survival, and risk factors. Gastroenterology Review. 2019;14(2):89–103. Available from: https://doi.org/10.5114/pg.2018.81072.

[5] Mohelnikova-Duchonova B. FOLFOX/FOLFIRI pharmacogenetics: The call for a personalized approach in colorectal cancer therapy. World Journal of Gastroenterology. 2014;20(30):10316. Available from: https://doi.org/10.3748/wjg.v20.i30.10316.

[6] Shulman K, Barnett-Griness O, Friedman V, Greenson JK, Gruber SB, Lejbkowicz F, et al. Outcomes of Chemotherapy for Microsatellite Instable–High Metastatic Colorectal Cancers. JCO Precision Oncology. 2018 Nov;(2):1–10. Available from: https://doi.org/10.1200/PO.17.00253.

[7] Boland CR, Thibodeau SN, Hamilton SR, Sidransky D, Eshleman JR, Burt RW, et al. A National Cancer Institute Workshop on Microsatellite Instability for cancer detection and familial predisposition: development of international criteria for the determination of microsatellite instability in colorectal cancer. Cancer Res. 1998 Nov;58(22):5248-57. Available from: https://pubmed.ncbi.nlm.nih.gov/9823339/.

[8] Sinicrope FA, Foster NR, Thibodeau SN, Marsoni S, Monges G, Labianca R, et al. DNA Mismatch Repair Status and Colon Cancer Recurrence and Survival in Clinical Trials of 5-Fluorouracil-Based Adjuvant Therapy. JNCI Journal of the National Cancer Institute. 2011 May;103(11):863–875. Available from: https://doi.org/10.1093/jnci/djr153.

[9] Venderbosch S, Nagtegaal ID, Maughan TS, Smith CG, Cheadle JP, Fisher D, et al. Mismatch Repair Status and BRAF Mutation Status in Metastatic Colorectal Cancer Patients: A Pooled Analysis of the CAIRO, CAIRO2, COIN, and FOCUS Studies. Clinical Cancer Research. 2014 Oct;20(20):5322–5330. Available from: https://doi.org/10.1158/1078-0432.CCR-14-0332.

[10] Fan WX, Su F, Zhang Y, Zhang XL, Du YY, Gao YJ, et al. Oncological characteristics, treatments and prognostic outcomes in MMR-deficient colorectal cancer. Biomarker Research. 2024 Aug;12(1). Available from: https://doi.org/10.1186/s40364-024-00640-7.

[11] André T, Shiu KK, Kim TW, Jensen BV, Jensen LH, Punt C, et al. Pembrolizumab in Microsatellite-Instability–High Advanced Colorectal Cancer. New England Journal of Medicine. 2020 Dec;383(23):2207–2218. Available from: https://doi.org/10.1056/NEJMoa2017699.

[12] Mulet-Margalef N, Linares J, Badia-Ramentol J, Jimeno M, Sanz Monte C, Manzano Mozo JL, et al. Challenges and Therapeutic Opportunities in the dMMR/MSI-H Colorectal Cancer Landscape. Cancers. 2023 Feb;15(4):1022. Available from: https://doi.org/10.3390/cancers15041022.

[13] Llosa NJ, Cruise M, Tam A, Wicks EC, Hechenbleikner EM, Taube JM, et al. The Vigorous Immune Microenvironment of Microsatellite Instable Colon Cancer Is Balanced by Multiple Counter-Inhibitory Checkpoints. Cancer Discovery. 2015 Jan;5(1):43–51. Available from: https://doi.org/10.1158/2159-8290.CD-14-0863.

[14] Giannakis M, Mu XJ, Shukla SA, Qian ZR, Cohen O, Nishihara R, et al. Genomic Correlates of Immune-Cell Infiltrates in Colorectal Carcinoma. Cell Reports. 2016 Apr;15(4):857–865. Available from: https://doi.org/10.1016/j.celrep.2016.03.075.

[15] Ciardiello D, Vitiello PP, Cardone C, Martini G, Troiani T, Martinelli E, et al. Immunotherapy of colorectal cancer: Challenges for therapeutic efficacy. Cancer Treatment Reviews. 2019 Jun;76:22–32. Available from: https://doi.org/10.1016/j.ctrv.2019.04.003.

[16] Topalian SL, Hodi FS, Brahmer JR, Gettinger SN, Smith DC, McDermott DF, et al. Safety, Activity, and Immune Correlates of Anti–PD-1 Antibody in Cancer. New England Journal of Medicine. 2012 Jun;366(26):2443–2454. Available from: https://doi.org/10.1056/NEJMoa1200690.

[17] Sarshekeh AM, Overman MJ, Kopetz S. Nivolumab in the Treatment of Microsatellite Instability High Metastatic Colorectal Cancer. Future Oncology. 2018 Feb;14(18):1869–1874. Available from: https://doi.org/10.2217/fon-2017-0696.

[18] Yaghoubi N, Soltani A, Ghazvini K, Hassanian SM, Hashemy SI. PD-1/ PD-L1 blockade as a novel treatment for colorectal cancer. Biomedicine & Pharmacotherapy. 2019 Feb;110:312–318. Available from: https://doi.org/10.1016/j.biopha.2018.11.105.

[19] Lin X, Kang K, Chen P, Zeng Z, Li G, Xiong W, et al. Regulatory mechanisms of PD-1/PD-L1 in cancers. Molecular Cancer. 2024 May;23(1). Available from: https://doi.org/10.1186/s12943-024-02023-w.

[20] Han Y, Liu D, Li L. PD-1/PD-L1 pathway: current researches in cancer. American journal of cancer research. 2020;10(3):727. Available from: https://pmc.ncbi.nlm.nih.gov/articles/PMC7136921/.

[21] Oliveira AF, Bretes L, Furtado I. Review of PD-1/PD-L1 Inhibitors in Metastatic dMMR/MSI-H Colorectal Cancer. Frontiers in Oncology. 2019 May;9. Available from: https://doi.org/10.3389/fonc.2019.00396.

[22] Lee J, Ahn E, Kissick HT, Ahmed R. Reinvigorating Exhausted T Cells by Blockade of the PD-1 Pathway. Forum on Immunopathological Diseases and Therapeutics. 2015;6(1–2):7–17. Available from: https://doi.org/10.1615/ForumImmunDisTher.2015014188.

[23] Zhang Y, Zhang Z. The history and advances in cancer immunotherapy: understanding the characteristics of tumor-infiltrating immune cells and their therapeutic implications. Cellular & Molecular Immunology. 2020 Jul;17(8):807–821. Available from: https://doi.org/10.1038/s41423-020-0488-6.

[24] Casak SJ, Marcus L, Fashoyin-Aje L, Mushti SL, Cheng J, Shen YL, et al. FDA Approval Summary: Pembrolizumab for the First-line Treatment of Patients with MSI-H/dMMR Advanced Unresectable or Metastatic Colorectal Carcinoma. Clinical Cancer Research. 2021 Apr;27(17):4680–4684. Available from: https://doi.org/10.1158/1078-0432.CCR-21-0557.

[25] Centanni M, Moes DJAR, Trocóniz IF, Ciccolini J, van Hasselt JGC. Clinical Pharmacokinetics and Pharmacodynamics of Immune Checkpoint Inhibitors. Clinical Pharmacokinetics. 2019 Feb;58(7):835–857. Available from: https://doi.org/10.1007/s40262-019-00748-2.

[26] Le Louedec F, Leenhardt F, Marin C, Chatelut E, Evrard A, Ciccolini J. Cancer Immunotherapy Dosing: A Pharmacokinetic/Pharmacodynamic Perspective. Vaccines. 2020 Oct;8(4):632. Available from: https://doi.org/10.3390/vaccines8040632.

[27] Kirshtein A, Akbarinejad S, Hao W, Le T, Su S, Aronow RA, et al. Data Driven Mathematical Model of Colon Cancer Progression. Journal of Clinical Medicine. 2020 Dec;9(12):3947. Available from: https://doi.org/10.3390/jcm9123947.

[28] Budithi A, Su S, Kirshtein A, Shahriyari L. Data Driven Mathematical Model of FOLFIRI Treatment for Colon Cancer. Cancers. 2021 May;13(11):2632. Available from: https://doi.org/10.3390/cancers13112632.

[29] Bozkurt F, Yousef A, Bilgil H, Baleanu D. A mathematical model with piecewise constant arguments of colorectal cancer with chemo-immunotherapy. Chaos, Solitons & Fractals. 2023 Mar;168:113207. Available from: https://doi.org/10.1016/j.chaos.2023.113207.

[30] dePillis L. Mathematical Model of Colorectal Cancer with Monoclonal Antibody Treatments. British Journal of Medicine and Medical Research. 2014 Jan;4(16):3101–3131. Available from: https://doi.org/10.9734/BJMMR/2014/8393.

[31] Lai X, Friedman A. Combination therapy of cancer with cancer vaccine and immune checkpoint inhibitors: A mathematical model. PLOS ONE. 2017 May;12(5):e0178479. Available from: https://doi.org/10.1371/journal.pone.0178479.

[32] Lai X, Friedman A. How to schedule VEGF and PD-1 inhibitors in combination cancer therapy? BMC Systems Biology. 2019 Mar;13(1). Available from: https://doi.org/10.1186/s12918-019-0706-y.

[33] Siewe N, Friedman A. TGF-β inhibition can overcome cancer primary resistance to PD-1 blockade: A mathematical model. PLOS ONE. 2021 Jun;16(6):e0252620. Available from: https://doi.org/10.1371/journal.pone.0252620.

[34] Siewe N, Friedman A. Cancer therapy with immune checkpoint inhibitor and CSF-1 blockade: A mathematical model. Journal of Theoretical Biology. 2023 Jan;556:111297. Available from: https://doi.org/10.1016/j.jtbi.2022.111297.

[35] Liao KL, Bai XF, Friedman A. IL-27 in combination with anti-PD-1 can be anti-cancer or pro-cancer. Journal of Theoretical Biology. 2024 Feb;579:111704. Available from: https://doi.org/10.1016/j.jtbi.2023.111704.

[36] Hawi G, Kim PS, Lee PP. Optimisation of neoadjuvant pembrolizumab therapy for locally advanced MSI-H/dMMR colorectal cancer using data-driven delay integro-differential equations; 2025. arXiv:2411.12123 [q-bio.CB]. Available from: https://doi.org/10.48550/arXiv.2411.12123.

[37] Wu T, Dai Y. Tumor microenvironment and therapeutic response. Cancer Letters. 2017 Feb;387:61–68. Available from: https://doi.org/10.1016/j.canlet.2016.01.043.

[38] Shah K, Al-Haidari A, Sun J, Kazi JU. T cell receptor (TCR) signaling in health and disease. Signal Transduction and Targeted Therapy. 2021 Dec;6(1). Available from: https://doi.org/10.1038/s41392-021-00823-w.

[39] Sugiyarto G, Lau D, Hill SL, Arcia-Anaya D, Boulanger DSM, Parkes EE, et al. Reactivation of low avidity tumor-specific CD8+ T cells associates with immunotherapeutic efficacy of anti-PD-1. Journal for ImmunoTherapy of Cancer. 2023 Aug;11(8):e007114. Available from: https://doi.org/10.1136/jitc-2023-007114.

[40] Maimela NR, Liu S, Zhang Y. Fates of CD8+ T cells in Tumor Microenvironment. Computational and Structural Biotechnology Journal. 2019;17:1–13. Available from: https://doi.org/10.1016/j.csbj.2018.11.004.

[41] Hoekstra ME, Vijver SV, Schumacher TN. Modulation of the tumor micro-environment by CD8+ T cell-derived cytokines. Current Opinion in Immunology. 2021 Apr;69:65–71. Available from: https://doi.org/10.1016/j.coi.2021.03.016.

[42] Caza T, Landas S. Functional and Phenotypic Plasticity of CD4+ T Cell Subsets. BioMed Research International. 2015;2015:1-13. Available from: https://doi.org/10.1155/2015/521957.

[43] Furiati SC, Catarino JS, Silva MV, Silva RF, Estevam RB, Teodoro RB, et al. Th1, Th17, and Treg Responses are Differently Modulated by TNF-α Inhibitors and Methotrexate in Psoriasis Patients. Scientific Reports. 2019 May;9(1). Available from: https://doi.org/10.1038/s41598-019-43899-9.

[44] Jarnicki AG, Lysaght J, Todryk S, Mills KHG. Suppression of Antitumor Immunity by IL-10 and TGF-β-Producing T Cells Infiltrating the Growing Tumor: Influence of Tumor Environment on the Induction of CD4+ and CD8+ Regulatory T Cells. The Journal of Immunology. 2006 Jul;177(2):896–904. Available from: https://doi.org/10.4049/jimmunol.177.2.896.

[45] Turnis ME, Sawant DV, Szymczak-Workman AL, Andrews LP, Delgoffe GM, Yano H, et al. Interleukin-35 Limits Anti-Tumor Immunity. Immunity. 2016 Feb;44(2):316–329. Available from: https://doi.org/10.1016/j.immuni.2016.01.013.

[46] Cui G. TH9, TH17, and TH22 Cell Subsets and Their Main Cytokine Products in the Pathogenesis of Colorectal Cancer. Frontiers in Oncology. 2019 Oct;9. Available from: https://doi.org/10.3389/fonc.2019.01002.

[47] Hetta HF, Elkady A, Yahia R, Meshall AK, Saad MM, Mekky MA, et al. T follicular helper and T follicular regulatory cells in colorectal cancer: A complex interplay. Journal of Immunological Methods. 2020 May;480:112753. Available from: https://doi.org/10.1016/j.jim.2020.112753.

[48] Kerneur C, Cano CE, Olive D. Major pathways involved in macrophage polarization in cancer. Frontiers in Immunology. 2022 Oct;13. Available from: https://doi.org/10.3389/fimmu.2022.1026954.

[49] Mills C. M1 and M2 Macrophages: Oracles of Health and Disease. Critical Reviews in Immunology. 2012;32(6):463-88. Available from: https://doi.org/10.1615/critrevimmunol.v32.i6.10.

[50] Viola A, Munari F, Sánchez-Rodríguez R, Scolaro T, Castegna A. The Metabolic Signature of Macrophage Responses. Frontiers in Immunology. 2019 Jul;10. Available from: https://doi.org/10.3389/fimmu.2019.01462.

[51] Han X, Ding S, Jiang H, Liu G. Roles of Macrophages in the Development and Treatment of Gut Inflammation. Frontiers in Cell and Developmental Biology. 2021 Mar;9. Available from: https://doi.org/10.3389/fcell.2021.625423.

[52] Xue J, Schmidt SV, Sander J, Draffehn A, Krebs W, Quester I, et al. Transcriptome-Based Network Analysis Reveals a Spectrum Model of Human Macrophage Activation. Immunity. 2014 Feb;40(2):274-88. Available from: https://doi.org/10.1016/j.immuni.2014.01.006.

[53] Wang Y, Zhu T, Shi Q, Zhu G, Zhu S, Hou F. Tumor-draining lymph nodes: opportunities, challenges, and future directions in colorectal cancer immunotherapy. Journal for ImmunoTherapy of Cancer. 2024 Jan;12(1):e008026. Available from: https://doi.org/10.1136/jitc-2023-008026.

[54] Newman AM, Steen CB, Liu CL, Gentles AJ, Chaudhuri AA, Scherer F, et al. Determining cell type abundance and expression from bulk tissues with digital cytometry. Nature Biotechnology. 2019 May;37(7):773–782. Available from: https://doi.org/10.1038/s41587-019-0114-2.

[55] Le T, Aronow RA, Kirshtein A, Shahriyari L. A review of digital cytometry methods: estimating the relative abundance of cell types in a bulk of cells. Briefings in Bioinformatics. 2020 Oct;22(4). Available from: https://doi.org/10.1093/bib/bbaa219.

[56] Gong T, Hartmann N, Kohane IS, Brinkmann V, Staedtler F, Letzkus M, et al. Optimal Deconvolution of Transcriptional Profiling Data Using Quadratic Programming with Application to Complex Clinical Blood Samples. PLoS ONE. 2011 Nov;6(11):e27156. Available from: https://doi.org/10.1371/journal.pone.0027156.

[57] Liebner DA, Huang K, Parvin JD. MMAD: microarray microdissection with analysis of differences is a computational tool for deconvoluting cell type-specific contributions from tissue samples. Bioinformatics. 2013 Oct;30(5):682–689. Available from: https://doi.org/10.1093/bioinformatics/btt566.

[58] Newman AM, Liu CL, Green MR, Gentles AJ, Feng W, Xu Y, et al. Robust enumeration of cell subsets from tissue expression profiles. Nature Methods. 2015 Mar;12(5):453–457. Available from: https://doi.org/10.1038/nmeth.3337.

[59] Miao YR, Zhang Q, Lei Q, Luo M, Xie GY, Wang H, et al. ImmuCellAI: A Unique Method for Comprehensive T-Cell Subsets Abundance Prediction and its Application in Cancer Immunotherapy. Advanced Science. 2020 Feb;7(7). Available from: https://doi.org/10.1002/advs.201902880.

[60] Goldman MJ, Craft B, Hastie M, Repečka K, McDade F, Kamath A, et al. Visualizing and interpreting cancer genomics data via the Xena platform. Nature Biotechnology. 2020 May;38(6):675–678. Available from: https://doi.org/10.1038/s41587-020-0546-8.

[61] Comprehensive molecular characterization of human colon and rectal cancer. Nature. 2012 Jul;487(7407):330–337. Available from: https://doi.org/10.1038/nature11252.

[62] Grossman RL, Heath AP, Ferretti V, Varmus HE, Lowy DR, Kibbe WA, et al. Toward a Shared Vision for Cancer Genomic Data. New England Journal of Medicine. 2016 Sep;375(12):1109–1112. Available from: https://doi.org/10.1056/NEJMp1607591.

[63] Kautto EA, Bonneville R, Miya J, Yu L, Krook MA, Reeser JW, et al. Performance evaluation for rapid detection of pan-cancer microsatellite instability with MANTIS. Oncotarget. 2016 Dec;8(5):7452–7463. Available from: https://doi.org/10.18632/oncotarget.13918.

[64] Wang X, Chen L, Liu W, Zhang Y, Liu D, Zhou C, et al. TIMEDB: tumor immune microenvironment cell composition database with automatic analysis and interactive visualization. Nucleic Acids Research. 2022 Nov;51(D1):D1417–D1424. Available from: https://doi.org/10.1093/nar/gkac1006.

[65] Sutton GJ, Poppe D, Simmons RK, Walsh K, Nawaz U, Lister R, et al. Comprehensive evaluation of deconvolution methods for human brain gene expression. Nature Communications. 2022 Mar;13(1). Available from: https://doi.org/10.1038/s41467-022-28655-4.

[66] Mao C, Chen Y, Xing D, Zhang T, Lin Y, Long C, et al. Resting natural killer cells promote the progress of colon cancer liver metastasis by elevating tumor-derived stem cell factor. eLife. 2024 Oct;13. Available from: https://doi.org/10.7554/eLife.97201.3.

[67] Sender R, Weiss Y, Navon Y, Milo I, Azulay N, Keren L, et al. The total mass, number, and distribution of immune cells in the human body. Proceedings of the National Academy of Sciences. 2023 Oct;120(44). Available from: https://doi.org/10.1073/pnas.2308511120.

[68] Maini R, Nagalli S. Lymphadenopathy. StatPearls Publishing, Treasure Island (FL); 2023. Available from: https://www.ncbi.nlm.nih.gov/books/NBK558918/.

[69] West H, Jin J. Lymph Nodes and Lymphadenopathy in Cancer. JAMA Oncology. 2016 Jul;2(7):971. Available from: https://doi.org/10.1001/jamaoncol.2015.3509.

[70] Burke JR, Brown P, Quyn A, Lambie H, Tolan D, Sagar P. Tumour growth rate of carcinoma of the colon and rectum: retrospective cohort study. BJS Open. 2020 Sep;4(6):1200–1207. Available from: https://doi.org/10.1002/bjs5.50355.

[71] Park JY, Kim SH, Lee SM, Lee JS, Han JK. CT volumetric measurement of colorectal cancer helps predict tumor staging and prognosis. PLOS ONE. 2017 Jun;12(6):e0178522. Available from: https://doi.org/10.1371/journal.pone.0178522.

[72] van Zijl F, Krupitza G, Mikulits W. Initial steps of metastasis: Cell invasion and endothelial transmigration. Mutation Research/Reviews in Mutation Research. 2011 Jul;728(1–2):23–34. Available from: https://doi.org/10.1016/j.mrrev.2011.05.002.

[73] Clough E, Barrett T. In: The Gene Expression Omnibus Database. Springer New York; 2016. p. 93–110. Available from: https://doi.org/10.1007/978-1-4939-3578-9_5.

[74] Barrett T, Wilhite SE, Ledoux P, Evangelista C, Kim IF, Tomashevsky M, et al. NCBI GEO: archive for functional genomics data sets—update. Nucleic Acids Research. 2012 Nov;41(D1):D991–D995. Available from: https://doi.org/10.1093/nar/gks1193.

[75] Leydold SM, Seewald M, Stratowa C, Kaserer K, Sommergruber W, Kraut N, et al. Peroxireduxin-4 is Over-Expressed in Colon Cancer and its Down-Regulation Leads to Apoptosis. Cancer Growth and Metastasis. 2011 Jan;4:CGM.S6584. Available from: https://doi.org/10.4137/CGM.S6584.

[76] Wang DY, Johnson DB, Davis EJ. Toxicities Associated With PD-1/PD-L1 Blockade. The Cancer Journal. 2018 Jan;24(1):36–40. Available from: https://doi.org/10.1097/PPO.0000000000000296.

[77] Martins F, Sofiya L, Sykiotis GP, Lamine F, Maillard M, Fraga M, et al. Adverse effects of immune-checkpoint inhibitors: epidemiology, management and surveillance. Nature Reviews Clinical Oncology. 2019 May;16(9):563–580. Available from: https://doi.org/10.1038/s41571-019-0218-0.

[78] Robert C, Schachter J, Long GV, Arance A, Grob JJ, Mortier L, et al. Pembrolizumab versus Ipilimumab in Advanced Melanoma. New England Journal of Medicine. 2015 Jun;372(26):2521–2532. Available from: https://doi.org/10.1056/NEJMoa1503093.

[79] Chatterjee M, Turner DC, Felip E, Lena H, Cappuzzo F, Horn L, et al. Systematic evaluation of pembrolizumab dosing in patients with advanced non-small-cell lung cancer. Annals of Oncology. 2016 Jul;27(7):1291–1298. Available from: https://doi.org/10.1093/annonc/mdw174.

[80] Merck. KEYTRUDA (pembrolizumab) injection Label; 2021. Available from: https://www.accessdata.fda.gov/drugsatfda_docs/label/2021/125514s096lbl.pdf.

[81] Wakiyama H, Kato T, Furusawa A, Okada R, Inagaki F, Furumoto H, et al. Treg-Dominant Tumor Microenvironment Is Responsible for Hyperprogressive Disease after PD-1 Blockade Therapy. Cancer Immunology Research. 2022 Oct;10(11):1386–1397. Available from: https://doi.org/10.1158/2326-6066.CIR-22-0041.

[82] Saleh R, Elkord E. Treg-mediated acquired resistance to immune checkpoint inhibitors. Cancer Letters. 2019 Aug;457:168–179. Available from: https://doi.org/10.1016/j.canlet.2019.05.003.

[83] Andre T, Lonardi S, Wong M, Lenz HJ, Gelsomino F, Aglietta M, et al. Nivolumab + ipilimumab combination in patients with DNA mismatch repair-deficient/microsatellite instability-high (dMMR/MSI-H) metastatic colorectal cancer (mCRC): First report of the full cohort from CheckMate-142. Journal of Clinical Oncology. 2018 Feb;36(4_suppl):553–553. Available from: https://doi.org/10.1200/JCO.2018.36.4_suppl.553.

[84] Overman MJ, Lonardi S, Wong KYM, Lenz HJ, Gelsomino F, Aglietta M, et al. Durable Clinical Benefit With Nivolumab Plus Ipilimumab in DNA Mismatch Repair–Deficient/Microsatellite Instability–High Metastatic Colorectal Cancer. Journal of Clinical Oncology. 2018 Mar;36(8):773–779. Available from: https://doi.org/10.1200/JCO.2017.76.9901.

[85] Bullock AJ, Schlechter BL, Fakih MG, Tsimberidou AM, Grossman JE, Gordon MS, et al. Botensilimab plus balstilimab in relapsed/refractory microsatellite stable metastatic colorectal cancer: a phase 1 trial. Nature Medicine. 2024 Jun;30(9):2558–2567. Available from: https://doi.org/10.1038/s41591-024-03083-7.

[86] Chand D, Savitsky DA, Krishnan S, Mednick G, Delepine C, Garcia-Broncano P, et al. Botensilimab, an Fc-Enhanced Anti–CTLA-4 Antibody, Is Effective against Tumors Poorly Responsive to Conventional Immunotherapy. Cancer Discovery. 2024 Jul;14(12):2407–2429. Available from: https://doi.org/10.1158/2159-8290.CD-24-0190.

[87] Bertrand A, Kostine M, Barnetche T, Truchetet ME, Schaeverbeke T. Immune related adverse events associated with anti-CTLA-4 antibodies: systematic review and meta-analysis. BMC Medicine. 2015 Sep;13(1). Available from: https://doi.org/10.1186/s12916-015-0455-8.

[88] Patnaik A, Kang SP, Rasco D, Papadopoulos KP, Elassaiss-Schaap J, Beeram M, et al. Phase I Study of Pembrolizumab (MK-3475; Anti–PD-1 Monoclonal Antibody) in Patients with Advanced Solid Tumors. Clinical Cancer Research. 2015 Sep;21(19):4286–4293. Available from: https://doi.org/10.1158/1078-0432.CCR-14-2607.

[89] Barua S, Fang P, Sharma A, Fujimoto J, Wistuba I, Rao AUK, et al. Spatial interaction of tumor cells and regulatory T cells correlates with survival in non-small cell lung cancer. Lung Cancer. 2018 Mar;117:73–79. Available from: https://doi.org/10.1016/j.lungcan.2018.01.022.

[90] Maley CC, Koelble K, Natrajan R, Aktipis A, Yuan Y. An ecological measure of immune-cancer colocalization as a prognostic factor for breast cancer. Breast Cancer Research. 2015 Sep;17(1). Available from: https://doi.org/10.1186/s13058-015-0638-4.

[91] Deenick EK, Gett AV, Hodgkin PD. Stochastic Model of T Cell Proliferation: A Calculus Revealing IL-2 Regulation of Precursor Frequencies, Cell Cycle Time, and Survival. The Journal of Immunology. 2003 May;170(10):4963–4972. Available from: https://doi.org/10.4049/jimmunol.170.10.4963.

[92] De Boer RJ, Ganusov VV, Milutinović D, Hodgkin PD, Perelson AS. Estimating Lymphocyte Division and Death Rates from CFSE Data. Bulletin of Mathematical Biology. 2006 May;68(5):1011–1031. Available from: https://doi.org/10.1007/s11538-006-9094-8.

[93] Kumbhari A, Egelston CA, Lee PP, Kim PS. Mature Dendritic Cells May Promote High-Avidity Tuning of Vaccine T Cell Responses. Frontiers in Immunology. 2020 Oct;11. Available from: https://doi.org/10.3389/fimmu.2020.584680.

[94] Kumbhari A, Rose D, Lee PP, Kim PS. A minimal model of T cell avidity may identify subtherapeutic vaccine schedules. Mathematical Biosciences. 2021 Apr;334:108556. Available from: https://doi.org/10.1016/j.mbs.2021.108556.

[95] Chung B, Stuge TB, Murad JP, Beilhack G, Andersen E, Armstrong BD, et al. Antigen-Specific Inhibition of High-Avidity T Cell Target Lysis by Low-Avidity T Cells via Trogocytosis. Cell Reports. 2014 Aug;8(3):871-82. Available from: https://doi.org/10.1016/j.celrep.2014.06.052.

[96] Curtsinger JM, Schmidt CS, Mondino A, Lins DC, Kedl RM, Jenkins MK, et al. Inflammatory Cytokines Provide a Third Signal for Activation of Naive CD4+ and CD8+ T Cells. The Journal of Immunology. 1999 Mar;162(6):3256–3262. Available from: https://doi.org/10.4049/jimmunol.162.6.3256.

[97] Raphael I, Nalawade S, Eagar TN, Forsthuber TG. T cell subsets and their signature cytokines in autoimmune and inflammatory diseases. Cytokine. 2015 Jul;74(1):5–17. Available from: https://doi.org/10.1016/j.cyto.2014.09.011.